Quaternion-based finite-element computation of nonlinear modes and frequency responses of geometrically exact beam structures in three dimensions

Marielle Debeurre, Aurélien Grolet, Olivier Thomas

Quaternion-based finite-element computation of nonlinear modes and frequency responses of geometrically exact beam structures in three dimensions

Marielle Debeurre[1] · Aurélien Grolet[1] · Olivier Thomas[1]

Abstract
In this paper, a novel method for computing the nonlinear dynamics of highly flexible slender structures in three dimensions (3D) is proposed. It is the extension to 3D of a previous work restricted to inplane (2D) deformations. It is based on the geometrically exact beam model, which is discretized with a finite-element method and solved entirely in the frequency domain with a harmonic balance method (HBM) coupled to an asymptotic numerical method (ANM) for continuation of periodic solutions. An important consideration is the parametrization of the rotations of the beam's cross sections, much more demanding than in the 2D case. Here, the rotations are parametrized with quaternions, with the advantage of leading naturally to polynomial nonlinearities in the model, well suited for applying the ANM. Because of the HBM–ANM framework, this numerical strategy is capable of computing both the frequency response of the structure under periodic oscillations and its nonlinear modes (namely its backbone curves and deformed shapes in free conservative oscillations). To illustrate and validate this strategy, it is used to solve two 3D deformations test cases of the literature: a cantilever beam and a clamped–clamped beam subjected to one-to-one (1:1) internal resonance between two companion bending modes in the case of a nearly square cross section.

Keywords Geometrically exact beam · Geometrical nonlinearities · Highly flexible structures · Quaternions · Large rotations · Nonlinear modes · 1:1 internal resonance

1 Introduction

In this work, a numerical strategy to compute in the frequency domain the nonlinear dynamics of highly flexible slender beam structures undergoing three-dimensional (3D) deformations is presented. This work is an extension of previous works: the work of Cottanceau *et al.*

✉ A. Grolet
aurelien.grolet@ensam.eu

M. Debeurre
marielle.debeurre@ensam.eu

O. Thomas
olivier.thomas@ensam.eu

[1] Arts et Métiers Institute of Technology, LISPEN, HESAM Université, F-59000 Lille, France

[1], which considered the 3D case in statics, and that of Debeurre *et al.* [2], which restricted the model to inplane deformations in dynamics. Highly flexible slender beam structures are commonly found in industrial applications with some examples including rulers, blades, and flexible wings, and also as elements of multibody systems. Proper modeling of highly flexible beams structures is paramount since these structures are capable of reaching very large amplitudes of motion owing to their unique geometry. It is characterized by one dimension of the structure (*e.g.,* the length) that is much larger than the other two dimensions (*e.g.,* the cross section), such that the resulting slender beam has a very low stiffness in bending and can easily deform up to very large amplitudes. In such cases, the so-called geometrically exact beam model is well adapted to model the large-amplitude motion of these structures since it exactly captures the arbitrarily large rotations of the structure's cross sections without restriction. In [2], a finite-element discretization of the geometrically exact beam model restricted to inplane motions (2D, restricted to inplane bending and axial motion) was derived and solved using a frequency domain-based numerical strategy combining the harmonic balance method (HBM) with the asymptotic numerical method (ANM) for continuation of periodic solutions. The present work proposes a natural extension to three-dimensional deformations, based on the same HBM–ANM strategy.

Accurate representation of the large-amplitude motion of highly flexible structures with the geometrically exact beam model has been a topic of increasing interest in recent decades. Based on the foundational work of Reissner [3, 4] and Simo and Vu-Quoc [5, 6], many works on the geometrically exact model have appeared in the literature [7–12]. Although different approaches to deriving the equations of motion can be found in the literature, the final partial differential equations are the same and all introduce a rotation operator. Differences then arise on how this rotation operator is parametrized (discussed more in the next paragraph) or on how the continuous equations are discretized and solved. Finite-element discretizations are most commonly found in the literature [7, 8, 11, 13–24], but other works utilize techniques such as finite differences [25, 26] or Galerkin techniques [27, 28]. The discrete equations can then be solved either with time integration or in the frequency domain. Many time domain-based geometrically exact models have been proposed in the literature [26, 29–34], but models solved with frequency-domain schemes are comparatively lacking. Frequency-domain solving schemes can be particularly advantageous in modeling the nonlinear dynamics of vibrating systems since they directly target the steady state of the periodic solution. The series of recent works by Farokhi *et al.* [27, 28, 35] on highly flexible beams proposed a frequency-domain solving scheme to target periodic motions, but the proposed model was limited in scope to cantilever beams. The topic of the current paper is to propose a frequency domain-based geometrically exact model for the modeling of any general beam structure.

The characteristic difficulty of geometrically exact models lies in treatment of the rotation terms [12]. Fixing the motion to the plane, as in [2, 36], allows for the single rotation degree of freedom to be parametrized with a rotation matrix in a straightforward way. With more rotation degrees of freedom under consideration, up to three for full 3D motion, rotation-matrix parametrization has some disadvantages, notably the presence of singularities at certain locations. Many alternative methods have therefore been proposed in the literature for the parametrization of rotations in 3D (see, e.g.,, [37]), some of which include Euler angles and Rodrigues parameters [38], unit quaternions [1, 25, 38–44] or a Lie group framework [24, 32–34, 45]. In this paper, we choose to parameterize the rotations in 3D using quaternions, in large part since they naturally lead to polynomial nonlinearities in the model, ideal for applying the ANM. Of particular interest (and that has not been done in the literature

to the knowledge of the authors) is solving a quaternion-based formulation of the geometrically exact beam model in the frequency domain in order to target periodic solutions of the equations of motion. This is precisely the aim of this work.

2 Beam equations in 3D

To begin, the geometrically exact beam equations are derived for motions in 3D in a way analogous to [2] for plane motions and to [1] for 3D deformations in statics. The derivation presented here is based on the formulation of Géradin and Cardona [38].

2.1 Beam kinematics in 3D

The geometry of the beam is reduced from the full nonlinear 3D continuum to a 1D continuum and is described by the series of cross sections through whose centroids passes a curve termed the "centerline" of the beam. This allows defining the geometrically exact beam model for which the displacement of any point in the cross section is computed based on the displacement of the centroid falling along the centerline of the beam in that same cross section. In three dimensions, 6 degrees of freedom are considered: 3 displacements or positions of the centerline in the 3 directions considered (the longitudinal direction and the two perpendicular transverse directions) and 3 rotations governing the orientation of the cross sections around these directions.

For this geometrically exact beam model, the main assumption is that the deformation of the cross sections is not considered, so that the cross sections are subjected to rigid-body motions when the beam deforms. In this work, Timoshenko kinematics is adopted, so that the effect of shearing is taken into account. This particular kinematics, which includes transverse shear effects, is known to have a larger application range in terms of slenderness of the geometry and/or of degree of the computed vibration modes, especially with respect to Euler–Bernoulli (EB) kinematics that neglects shearing (also known as Kirchhoff theory of rods [11]). However, in this paper, we are interested only in the first low-frequency nonlinear modes of very slender beams, cases for which EB kinematics would be entirely suitable. Our choice of Timoshenko kinematics is thus not dictated by the application range of the theory, but because it enables low-order. finite-element discretizations (EB kinematics requires at least 3rd-order finite elements, whereas 2nd-order ones are used here, see §4.1). Moreover, with EB kinematics, the rotation of the cross section must be linked to the transverse displacement field, which in this case would not be straightforward because of the sine/cosine relations between the quaternions and the cross-sectional rotation.

Consider an elementary portion of a beam illustrated in Fig. 1 for which the initial (undeformed and unstressed, reference) configuration can be curved (its centerline is not straight). Its geometry is defined by the position vector $\mathbf{X}_0(s) = \mathbf{OC}'$ of the points C' of the centerline, $s \in \mathbb{R}$ being a curvilinear parameter and O the origin of a fixed (right-handed orthonormal) *global frame* $(O, \mathbf{u}_x, \mathbf{u}_y, \mathbf{u}_z)$. Each cross section is orthogonal to the centerline, such that we define a (right-handed orthonormal) local basis $(\mathbf{E}_x(s), \mathbf{E}_y(s), \mathbf{E}_z(s))$, with $\mathbf{E}_x(s)$ tangent to the centerline in $C'(s)$. Then, the position of any point P' of the cross section is defined by the vector $\mathbf{C'P'} = y\mathbf{E}_y + z\mathbf{E}_z$, $(y, z) \in \mathcal{S} \subset \mathbb{R}^2$ being the coordinates of P' in the cross section of domain $\mathcal{S}$.

The possibly curved geometry of the initial configuration is defined by the orientation of the basis $(\mathbf{E}_x(s), \mathbf{E}_y(s), \mathbf{E}_z(s))$ with respect to the global basis $(\mathbf{u}_x, \mathbf{u}_y, \mathbf{u}_z)$, defined by

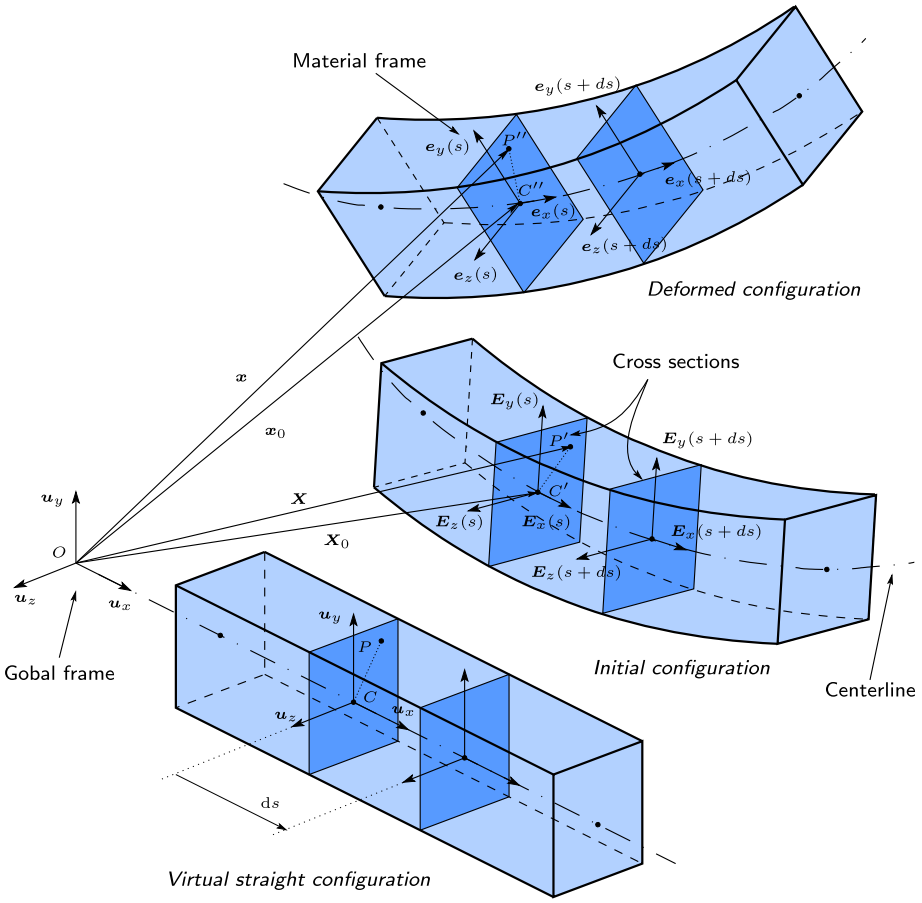

Fig. 1 3D beam kinematics (Color figure online)

a rotation operator $\mathbf{R}_0(s)$ such that $\left(\mathbf{E}_x(s), \mathbf{E}_y(s), \mathbf{E}_z(s)\right) = \mathbf{R}_0(s)\left(\mathbf{u}_x, \mathbf{u}_y, \mathbf{u}_z\right)$. As a consequence, $\mathbf{C'P'} = \mathbf{R}_0\mathbf{CP}$ and:

$$\mathbf{X}(s, y, z) = \mathbf{X}_0(s) + \mathbf{R}_0(s)\mathbf{CP}. \tag{1}$$

As any cross section of the beam undergoes a rigid-body motion during deformation, the same logic is kept for defining the deformed (current) configuration of the beam. The deformed centerline is defined by the vector $\mathbf{x}_0(s) = \mathbf{OC}''$. The orientation of the cross section is defined by a (right-handed orthonormal) *material basis* $\left(\mathbf{e}_x(s), \mathbf{e}_y(s), \mathbf{e}_z(s)\right)$, with $\mathbf{e}_x$ normal to the deformed cross section at point C''. Note that $\mathbf{e}_x$ is not necessarily tangent to the deformed centerline at C'' because of the Timoshenko kinematics that allows for transverse shearing. The orientation of this basis is defined with respect to the virtual straight configuration by the rotation operator $\mathbf{R}(s)$, such that $\left(\mathbf{e}_x(s), \mathbf{e}_y(s), \mathbf{e}_z(s)\right) = \mathbf{R}(s)\left(\mathbf{u}_x, \mathbf{u}_y, \mathbf{u}_z\right)$. The position of any point P'' of the deformed configuration is then:

$$\mathbf{x}(s, y, z) = \mathbf{x}_0(s) + \mathbf{R}(s)\mathbf{CP}. \tag{2}$$

As a consequence, the position of any point in the deformed configuration is governed by the two fields $\mathbf{x}_0(s)$ and $\mathbf{R}(s)$. The 3 positions in $\mathbf{x}_0(s)$ and the 3 rotations governed by $\mathbf{R}(s)$, then, constitute the 6 aforementioned degrees of freedom of the 1D beam model.

If necessary, the displacement field of the centerline between the initial and deformed configurations can be defined by:

$$\mathbf{u}_0 = \mathbf{x}_0 - \mathbf{X}_0. \tag{3}$$

Note that in the 2D model of [2, 36], the displacements are used as the degrees of freedom in the governing equations, while in [1] the positions are used in the derivation of the governing equations. For convenience, and in order to remain consistent with the formulation of Cottanceau *et al.* [1], the equations are derived in what follows based on the centerline positions $\mathbf{x}_0$, but they can be easily rewritten in terms of the associated displacements $\mathbf{u}_0$ using the relation Eq. (3) (see also [38] for derivations of the equations based on both $\mathbf{x}$ and $\mathbf{u}_0$).

2.2 Strain measures

In this work, the classical strain measures for the geometrically exact beam are used. They can be decomposed into two parts [38]: the material measure of deformation of the neutral axis, denoted $\boldsymbol{\Gamma} = [\Gamma_x, \Gamma_y, \Gamma_z]^{\mathrm{T}}$ (axial strain Γ_x and the two polarizations of shear strains Γ_y and Γ_z), and the material measure of curvature related to rotations of the cross section, denoted $\mathbf{K} = [\kappa_x, \kappa_y, \kappa_z]^{\mathrm{T}}$ (torsional curvature κ_x and the two polarizations of bending curvature κ_y and κ_z). These vectors, with components in the material frame, are obtained according to:

$$\boldsymbol{\Gamma} = \mathbf{R}^{\mathrm{T}}\mathbf{x}_0' - \mathbf{R}_0^{\mathrm{T}}\mathbf{X}_0' = \mathbf{R}^{\mathrm{T}}\mathbf{x}_0' - \boldsymbol{\Gamma}_0, \tag{4a}$$

$$\mathbf{K} = \mathrm{vect}\left(\mathbf{R}^{\mathrm{T}}\mathbf{R}' - \mathbf{R}_0^{\mathrm{T}}\mathbf{R}_0'\right) = \mathrm{vect}\left(\mathbf{R}^{\mathrm{T}}\mathbf{R}'\right) - \mathbf{K}_0, \tag{4b}$$

where $(\diamond)' = \partial(\diamond)/\partial s$ and the vect operator indicates a transformation from a 3×3 skew-symmetric matrix to a 3-component vector:

$$\widetilde{\mathbf{a}} = \begin{bmatrix} 0 & -a_3 & a_2 \\ a_3 & 0 & -a_1 \\ -a_2 & a_1 & 0 \end{bmatrix} \quad \Leftrightarrow \quad \mathbf{a} = \mathrm{vect}(\widetilde{\mathbf{a}}) = \begin{bmatrix} a_1 \\ a_2 \\ a_3 \end{bmatrix}. \tag{5}$$

$\boldsymbol{\Gamma}_0$ and $\mathbf{K}_0$ represent, respectively, the initial deformation and initial curvatures of the beam in the unloaded configuration. These terms can be computed from the initial configuration as $\boldsymbol{\Gamma}_0 = \mathbf{R}_0^T\mathbf{X}_0'$ and $\mathbf{K}_0 = \mathbf{R}_0^T\mathbf{R}_0'$.

Equations (4a)–(4b) can be obtained in several ways. In so-called Cosserat theories, they are derived by differentiation of $\mathbf{x}$, $\mathbf{R}$, $\mathbf{x}_0$, and $\mathbf{R}_0$ with respect to s [38, 46]. They can also be obtained as the strain measures energetically conjugated to the generalized internal stresses (internal forces and moments), as originally introduced by Reissner [3, 4, 7]. Finally, they are also the result of a more direct continuum mechanics procedure since they appear in the tensor components of a consistent linearization of the Green–Lagrange strain tensor by use of a pseudopolar decomposition of the deformation gradient (see [36] in the 2D case for initially straight configuration, [38] for the 3D case and [11, 47, 48] for an arbitrary curved initial configuration). This consistent linearization allows for the second-order terms in the strains, independent of the cross-sectional rotation that is kept exact, to be neglected. These strain measures appear to coincide with Biot strain measures [36, 49].

For the sake of simplicity, in the remainder of the paper only initially straight beams whose centerlines are aligned with the $\mathbf{u}_x$-axis in the initial configuration are considered. In this case, $\mathbf{R}_0 = \mathbf{I}_d$, *i.e.,* $\big(\mathbf{E}_x(s), \mathbf{E}_y(s), \mathbf{E}_z(s)\big) = \big(\mathbf{u}_x, \mathbf{u}_y, \mathbf{u}_z\big)$ and the computation of the initial strain and curvature is straightforward, leading to:

$$\boldsymbol{\Gamma}_0 = \mathbf{u}_1 = \begin{bmatrix} 1 \\ 0 \\ 0 \end{bmatrix} \quad \text{and} \quad \mathbf{K}_0 = \mathbf{0}. \tag{6}$$

2.3 Constitutive law

Each cross section is subjected to an internal force vector $\mathbf{N}(s)$ and moment vector $\mathbf{M}(s)$ (expressed in the material frame) that correspond to the integral over the cross section of the Biot stresses [36]. In this work, the stresses are related to the strains according to a linear elastic Kirchhoff–Saint-Venant constitutive law for homogeneous and isotropic materials as in [2]. This leads to a linear relation between the internal forces $(\mathbf{N}, \mathbf{M})$ and the strains $(\boldsymbol{\Gamma}, \mathbf{K})$ according to the following constitutive relation:

$$\mathbf{N} = \mathbf{C}_N \boldsymbol{\Gamma} \quad \text{and} \quad \mathbf{M} = \mathbf{C}_M \mathbf{K}, \tag{7}$$

where the 3×3 diagonal matrices $\mathbf{C}_N$ and $\mathbf{C}_M$ are given as:

$$\mathbf{C}_N = \operatorname{diag}\big(EA, \quad k_y GA, \quad k_z GA\big) \quad \text{and} \quad \mathbf{C}_M = \operatorname{diag}\big(GJ, \quad EI_y, \quad EI_z\big), \tag{8}$$

where A is the area of the cross section, E is Young's modulus, $G = E/[2(1+\nu)]$ is the shear modulus (ν is Poisson's ratio), k_y and k_z are the shear correction coefficients in directions $\mathbf{e}_y$ and $\mathbf{e}_z$, J is the polar second moment of area (that can include warping effects for twisting deformations), and I_y, I_z are the second moments of area in the $\mathbf{e}_y$ and $\mathbf{e}_z$ directions. If the cross section of the beam is variable, then the matrices $\mathbf{C}_N$ and $\mathbf{C}_M$ depend on the position along the beam. In the remainder of this work, only beams with constant cross sections are considered, so that the matrices $\mathbf{C}_N$ and $\mathbf{C}_M$ remain constant.

2.4 Computation of the variations

In this section, computation of the variations of the various terms is discussed, variations that are needed in the derivation of the equations of motions are discussed in Sect. 2.5.

2.4.1 Variation of the rotation operator

In the remainder of this section, we will consider a classical parametrization for the rotation operator $\mathbf{R} \in \mathrm{SO}(3)$ using three angles of rotation [37]. The variation of the rotation operator, denoted $\delta\mathbf{R}$, can be expressed using Lie group theory [38] as:

$$\delta\mathbf{R} = \mathbf{R}\delta\widetilde{\boldsymbol{\Theta}}, \tag{9}$$

where $\delta\widetilde{\boldsymbol{\Theta}}$ is a 3×3 skew-symmetric matrix (an element of the Lie algebra of the rotation group SO(3)) that can be converted to a 3×1 vector $\delta\boldsymbol{\Theta}$ by the definition:

$$\delta\boldsymbol{\Theta} = \operatorname{vect}(\delta\widetilde{\boldsymbol{\Theta}}). \tag{10}$$

The vector $\delta\boldsymbol{\Theta}$ corresponds to an infinitesimal angular displacement, with components in the material frame. This infinitesimal angular variation vector can also be expressed in the global frame (denoted by $\delta\boldsymbol{\theta}$) by using the following transformation:

$$\delta\boldsymbol{\theta} = \mathbf{R}\delta\boldsymbol{\Theta}. \tag{11}$$

2.4.2 Variations of the strains and curvature

Consider first the variation of the strains denoted $\delta\boldsymbol{\Gamma}$. Using the definition in Eq. (4a)–(4b), Eq. (9), and the fact that the cross (vector) product of two vectors is equivalent to the multiplication with a skew-symmetric matrix as:

$$\mathbf{a} \times \mathbf{b} = \widetilde{\mathbf{a}}\,\mathbf{b}, \quad \forall \mathbf{a}, \mathbf{b} \in \mathbb{R}^3, \tag{12}$$

the variation is computed as:

$$\delta\boldsymbol{\Gamma} = (\boldsymbol{\Gamma} + \boldsymbol{\Gamma}_0) \times \delta\boldsymbol{\Theta} + \mathbf{R}^T \delta\mathbf{x}_0'. \tag{13}$$

Next, the variation of the curvature $\delta\mathbf{K}$ is obtained by equating the derivative $(\delta\mathbf{R})'$ with the variation $\delta(\mathbf{R}')$. This leads to the following relation, expressed in terms of 3×3 skew-symmetric matrices as:

$$\delta\tilde{\mathbf{K}} = \delta\tilde{\boldsymbol{\Theta}}' + \tilde{\mathbf{K}}\delta\tilde{\boldsymbol{\Theta}} - \delta\tilde{\boldsymbol{\Theta}}\tilde{\mathbf{K}}. \tag{14}$$

The above relation can be expressed in terms of 3×1 vectors, leading to the following expression for the variation of the curvature vector:

$$\delta\mathbf{K} = \delta\boldsymbol{\Theta}' + \mathbf{K} \times \delta\boldsymbol{\Theta}. \tag{15}$$

2.4.3 Velocity and acceleration fields

By replacing the variation operator δ with the differential operator d, the variation of the rotation operator can be used to compute the derivation of the rotation matrix with relation to time t: $\dot{\mathbf{R}} = \partial\mathbf{R}/\partial t = \mathbf{R}\widetilde{\boldsymbol{\Omega}}$, leading to the definition of the rotation velocity matrix $\widetilde{\boldsymbol{\Omega}} = \partial\widetilde{\boldsymbol{\Theta}}/\partial t = \mathbf{R}^{\mathbf{T}}\dot{\mathbf{R}}$, associated to the rotation velocity vector $\boldsymbol{\Omega}$ (expressed in the material frame):

$$\boldsymbol{\Omega} = \mathrm{vect}(\widetilde{\boldsymbol{\Omega}}) = \mathrm{vect}(\mathbf{R}^T\dot{\mathbf{R}}) = \frac{\partial\boldsymbol{\Theta}}{\partial t}. \tag{16}$$

Using the transformation definition in Eq. (2) and the variation of the rotation matrix as presented in Sect. 2.4.1, the velocity $\dot{\mathbf{x}}$ of a point P of the beam is written (w.r.t. the global frame):

$$\dot{\mathbf{x}} = \dot{\mathbf{x}}_0 + \dot{\mathbf{R}}\,\mathbf{CP} = \dot{\mathbf{x}}_0 + \mathbf{R}\,\widetilde{\boldsymbol{\Omega}}\,\mathbf{CP} = \dot{\mathbf{x}}_0 + \mathbf{R}\,(\boldsymbol{\Omega} \times \mathbf{CP}), \tag{17}$$

where $\widetilde{\boldsymbol{\Omega}}$ is the rotation velocity matrix and $\boldsymbol{\Omega}$ is the associated rotation velocity vector. The acceleration field $\ddot{\mathbf{x}}$ (w.r.t. the global frame) is then found as:

$$\begin{aligned}\ddot{\mathbf{x}} &= \ddot{\mathbf{x}}_0 + \dot{\mathbf{R}}\,\widetilde{\boldsymbol{\Omega}}\,\mathbf{CP} + \mathbf{R}\,\dot{\widetilde{\boldsymbol{\Omega}}}\,\mathbf{CP} = \ddot{\mathbf{x}}_0 + \mathbf{R}\,\widetilde{\boldsymbol{\Omega}}^2\,\mathbf{CP} + \mathbf{R}\,\dot{\widetilde{\boldsymbol{\Omega}}}\,\mathbf{CP} \\ &= \ddot{\mathbf{x}}_0 + \mathbf{R}\,\left[\boldsymbol{\Omega} \times (\boldsymbol{\Omega} \times \mathbf{CP}) + \dot{\boldsymbol{\Omega}} \times \mathbf{CP}\right],\end{aligned} \tag{18}$$

where $\dot{\boldsymbol{\Omega}}$ is the vector of angular acceleration (given in the material frame).

As explained in §2.1, this work aims at computing the response of very slender structures around their first low-frequency resonances. In this situation, in the case of a linear model, the rotary inertia is known to play a negligible role and is often neglected when using Euler–Bernoulli kinematics. This is justified by analyzing the dispersion curves of bending waves for several models (see [50] for beams and [51] for plates), showing that the rotary inertia correction is of a higher order than the correction due to the inclusion of transverse shearing. The same conclusion applies to geometrically nonlinear beams as analyzed in [52]. An empirical justification for this choice is also provided in B, which demonstrates that there is no noticeable difference in the backbone curve of the first mode of a cantilever beam with and without inclusion of the rotary inertia. For these reasons, and because it simplifies the computations by yielding solely linear inertia forces in the discretized model, we therefore choose to neglect the rotary inertia of the cross sections. In this case, the expression for the acceleration field simplifies to:

$$\ddot{\mathbf{x}} = \ddot{\mathbf{x}}_0. \tag{19}$$

2.5 Principle of virtual work and weak form of the equations of motion

In this section, the weak form of the geometrically exact beam equations of motion is derived by making use of the principle of virtual work. It states that for any virtual variation of the displacement fields $\delta\mathbf{x}$, the sum of the virtual work of the internal forces and the virtual work of the external forces is equal to the virtual work of the inertial (acceleration) forces:

$$\delta W_i + \delta W_e = \delta W_a \quad \forall \delta\mathbf{x}, \tag{20}$$

where δW_a is the virtual work of the inertial forces, δW_i that of the internal forces, and δW_e that of the external forces.

Following the definition of the displacement field $\mathbf{x}$ given in Eq. (2), it can be seen that the variation $\delta\mathbf{x}$ involves the variation of the centerline displacement $\delta\mathbf{x}_0$ and the variation of the rotation matrix $\delta\mathbf{R}$ (or equivalently the angular variation vector $\delta\boldsymbol{\Theta}$). The variation is expressed as follows:

$$\delta\mathbf{x} = \delta\mathbf{x}_0 + \delta\mathbf{R}\,\mathbf{CP} = \delta\mathbf{x}_0 + \mathbf{R}\delta\tilde{\boldsymbol{\Theta}}\mathbf{CP} = \delta\mathbf{x}_0 + \mathbf{R}(\delta\boldsymbol{\Theta} \times \mathbf{CP}). \tag{21}$$

Based on the kinematics of the geometrically exact beam (Sect. 2.1), after integration over the cross section the virtual works of Eq. (20) are written as [38]:

$$\begin{aligned}\delta W_a &= \int_V \ddot{\mathbf{x}}^T \delta\mathbf{x}\, dV = \int_0^L \left(\rho A \ddot{\mathbf{x}}_0^{\mathrm{T}} \delta\mathbf{x}_0\right) \mathrm{d}s + \int_0^L \left((\mathbf{J}\dot{\boldsymbol{\Omega}} + \boldsymbol{\Omega} \times (\mathbf{J}\boldsymbol{\Omega}))^{\mathrm{T}} \delta\boldsymbol{\Theta}\right) \mathrm{d}s \\ &\approx \int_0^L \left(\rho A \ddot{\mathbf{x}}_0^{\mathrm{T}} \delta\mathbf{x}_0\right) \mathrm{d}s, \end{aligned} \tag{22a}$$

$$\delta W_i = -\int_0^L \left(\mathbf{N}^{\mathrm{T}} \delta\boldsymbol{\Gamma} + \mathbf{M}^{\mathrm{T}} \delta\mathbf{K}\right) \mathrm{d}s, \tag{22b}$$

$$\delta W_e = \int_0^L \left(\mathbf{n}_e^{\mathrm{T}} \delta\mathbf{x}_0 + \mathbf{m}_e^{\mathrm{T}} \delta\boldsymbol{\theta}\right) \mathrm{d}s + \left[\mathbf{f}_e^{\mathrm{T}} \delta\mathbf{x}_0\right]_0^L + \left[\mathbf{c}_e^{\mathrm{T}} \delta\boldsymbol{\theta}\right]_0^L, \tag{22c}$$

where L is the length of the beam, A is the area of the cross section, ρ is the density of the material, $\mathbf{J}$ is the inertia tensor of the cross section (expressed in the material basis); $\mathbf{n}_e$

and $\mathbf{m}_e$ are the external forces and moments per unit length applied on the current configuration; $\mathbf{f}_e$ and $\mathbf{c}_e$ are the external applied force and moment at the boundaries of the beam in the current configuration, in $s = 0, L$; $\delta\mathbf{x}_0$ is the displacement variation of the center line; $\delta\boldsymbol{\Theta}$ and $\delta\boldsymbol{\theta} = \mathbf{R}\delta\boldsymbol{\Theta}$ are the variation of angular displacements, expressed, respectively, in the material basis and in the global basis. These last two vectors are required since some variables are naturally expressed in the material frame ($\mathbf{N}$, $\mathbf{M}$, $\boldsymbol{\Gamma}$, $\mathbf{K}$, $\boldsymbol{\Omega}$), whereas others are naturally expressed in the global frame ($\mathbf{n}_e$, $\mathbf{m}_e$, $\mathbf{f}_e$, $\mathbf{c}_e$).

The weak form of the equations of motion for the geometrically exact beam is then derived by substituting the expressions for the variations into the principle of virtual work (and neglecting rotational inertia):

$$\begin{aligned}\int_0^L &\left[\mathbf{N}^T\mathbf{R}^T\delta\mathbf{x}_0' + \left(\rho A\ddot{\mathbf{x}}_0^{\mathrm{T}} - \mathbf{n}_e^T\right)\delta\mathbf{x}_0 + \mathbf{M}^{\mathrm{T}}\delta\boldsymbol{\Theta}' + \left((\mathbf{N}\times(\boldsymbol{\Gamma}+\boldsymbol{\Gamma}_0))^T\right.\right.\\ &\left.\left.+ (\mathbf{M}\times\mathbf{K})^T - \mathbf{m}_e^T\mathbf{R}\right)\delta\boldsymbol{\Theta}\right]\mathrm{d}s\\ &+ \left[\mathbf{f}_e^{\mathrm{T}}\delta\mathbf{x}_0\right]_0^L + \left[\mathbf{c}_e^{\mathrm{T}}\mathbf{R}\delta\boldsymbol{\Theta}\right]_0^L = 0,\end{aligned} \tag{23}$$

which can be rewritten in the form of a dot product as:

$$\begin{aligned}\int_0^L &\begin{bmatrix}\mathbf{RN}\\ \rho A\ddot{\mathbf{x}}_0 - \mathbf{n}_e\\ \mathbf{M}\\ \left(\mathbf{N}\times(\boldsymbol{\Gamma}+\boldsymbol{\Gamma}_0) + \mathbf{M}\times\mathbf{K} - \mathbf{R}^T\mathbf{m}_e\right)\end{bmatrix}^T \begin{bmatrix}\delta\mathbf{x}_0'\\ \delta\mathbf{x}_0\\ \delta\boldsymbol{\Theta}'\\ \delta\boldsymbol{\Theta}\end{bmatrix}\mathrm{d}s + \left[\mathbf{f}_e^{\mathrm{T}}\delta\mathbf{x}_0\right]_0^L\\ &+ \left[(\mathbf{R}^{\mathrm{T}}\mathbf{c}_e)^{\mathrm{T}}\delta\boldsymbol{\Theta}\right]_0^L = 0.\end{aligned} \tag{24}$$

3 Rotation parametrization with quaternions

In this section, the selected method for parametrization of rotations in 3D is introduced, which consists in using unit quaternions. After presenting some generalities regarding quaternions and this method of rotation representation, the weak form of the equations of motion as derived in Eq. (24) is rewritten using this parametrization style.

3.1 Definition and basic properties of the quaternion algebra

Some basic properties of quaternion algebra used in the remainder of this paper are presented in this section. The interested reader is referred to [38, 39, 42, 53] (and the references cited therein) for more details on the mathematics of quaternion algebra.

The quaternions set, denoted $\mathbb{H}$, forms a noncommutative algebra of dimension 4 that is spanned by the basis $(1,\ i,\ j,\ k)$ with the properties $i^2 = j^2 = k^2 = ijk = -1$, see, *e.g.,* [39]. In what follows, quaternion quantities are represented using the hat symbol $\hat{\diamond}$. A quaternion $\widehat{\mathbf{q}}$ can be seen as a "4-dimensional complex number," represented by the sum of a scalar part (q_0) and vector part ($\mathbf{q} = \begin{bmatrix}q_1 & q_2 & q_3\end{bmatrix}^{\mathrm{T}}$) as:

$$\hat{\mathbf{q}} = q_0 + \mathbf{q} = q_0 + q_1 i + q_2 j + q_3 k. \tag{25}$$

In quaternion algebra there exists an involution, equivalent to taking the conjugate of a quaternion and indicated with the asterisk $\diamond^*$, such that for any general quaternion $\hat{\mathbf{q}}$, $\hat{\mathbf{q}}^*$ is

defined as:

$$\hat{\mathbf{q}}^* = q_0 - \mathbf{q}. \tag{26}$$

Quaternion addition is straightforward and can be seen as the addition of vectors of $\mathbb{R}^4$. On the other hand, quaternion multiplication is more complex and is defined for two quaternions $\hat{\mathbf{p}}$ and $\hat{\mathbf{q}}$ as a consequence of a standard multiplication of two quaternions defined by Eq. (25) along with the properties of (i, j, k). It is denoted by $\hat{\mathbf{p}}\,\hat{\mathbf{q}}$ and defined as:

$$\hat{\mathbf{p}}\,\hat{\mathbf{q}} = (p_0 q_0 - \mathbf{p}\cdot\mathbf{q}) + (q_0\mathbf{p} + p_0\mathbf{q} + \mathbf{p}\times\mathbf{q}), \tag{27}$$

where $\mathbf{p}\cdot\mathbf{q}$ (resp., $\mathbf{p}\times\mathbf{q}$) is the dot product (resp., the cross product) of vectors of $\mathbb{R}^3$. Note that quaternion multiplication is noncommutative (*i.e.,* in general $\hat{\mathbf{p}}\,\hat{\mathbf{q}} \neq \hat{\mathbf{q}}\,\hat{\mathbf{p}}$).

To carry out computations in practice, it can be convenient to use a 4×1 vector to represent a quaternion, *e.g.,* $\hat{\mathbf{q}} = \begin{bmatrix} q_0 & q_1 & q_2 & q_3 \end{bmatrix}^{\mathrm{T}} = \begin{bmatrix} q_0 & \mathbf{q}^{\mathrm{T}} \end{bmatrix}^{\mathrm{T}}$. This is the approach used in the code developed in this work and tested later in Sect. 5. In this case, quaternion multiplications are carried out as matrix multiplications making use of the transformations denoted Φ_L and Φ_R ("left" and "right" multiplications, respectively), such that the multiplication of quaternions is represented in the following way:

$$\begin{aligned}
\hat{\mathbf{a}}\,\hat{\mathbf{b}} = \Phi_L(\hat{\mathbf{a}})\hat{\mathbf{b}} &= \begin{bmatrix} a_0 & -\mathbf{a}^{\mathrm{T}} \\ \mathbf{a} & a_0\mathbf{I}_3 + \tilde{\mathbf{a}} \end{bmatrix}\begin{bmatrix} b_0 \\ \mathbf{b} \end{bmatrix} \\
&= \begin{bmatrix} a_0 & -a_1 & -a_2 & -a_3 \\ a_1 & a_0 & -a_3 & a_2 \\ a_2 & a_3 & a_0 & -a_1 \\ a_3 & -a_2 & a_1 & a_0 \end{bmatrix}\begin{bmatrix} b_0 \\ b_1 \\ b_2 \\ b_3 \end{bmatrix},
\end{aligned} \tag{28a}$$

$$\begin{aligned}
\hat{\mathbf{a}}\,\hat{\mathbf{b}} = \Phi_R(\hat{\mathbf{b}})\hat{\mathbf{a}} &= \begin{bmatrix} b_0 & -\mathbf{b}^{\mathrm{T}} \\ \mathbf{b} & b_0\mathbf{I}_3 - \tilde{\mathbf{b}} \end{bmatrix}\begin{bmatrix} a_0 \\ \mathbf{a} \end{bmatrix} \\
&= \begin{bmatrix} b_0 & -b_1 & -b_2 & -b_3 \\ b_1 & b_0 & b_3 & -b_2 \\ b_2 & -b_3 & b_0 & b_1 \\ b_3 & b_2 & -b_1 & b_0 \end{bmatrix}\begin{bmatrix} a_0 \\ a_1 \\ a_2 \\ a_3 \end{bmatrix},
\end{aligned} \tag{28b}$$

where $\tilde{\mathbf{a}}$ and $\tilde{\mathbf{b}}$ are the 3×3 skew-symmetric matrices associated to the 3×1 vectors $\mathbf{a}$ and $\mathbf{b}$. The norm of a quaternion can be defined as $|\hat{\mathbf{q}}| = \sqrt{\hat{\mathbf{q}}^*\,\hat{\mathbf{q}}} = \sqrt{\hat{\mathbf{q}}\cdot\hat{\mathbf{q}}}$, where $\hat{\mathbf{q}}\cdot\hat{\mathbf{q}}$ is the regular dot product of vectors of $\mathbb{R}^4$.

In the special case where the scalar part of the quaternion $\hat{\mathbf{q}}$ is zero (*i.e.,* $q_0 = 0$), $\hat{\mathbf{q}}$ is called a pure quaternion (also called a vector quaternion). Pure quaternions are images of the natural injection of $\mathbb{R}^3$ into $\mathbb{H}$ such that a pure quaterion $\hat{\mathbf{q}} = 0\cdot 1 + \mathbf{q}$ is associated to a 3×1 vector $\mathbf{q}$. Conversely, a pure quaternion (or actually any quaternion) can be projected from $\mathbb{H}$ to $\mathbb{R}^3$ through the operation defined here as $\mathrm{vec}(\diamond) : \mathbb{H} \mapsto \mathbb{R}^3$, so that $\mathrm{vec}(\hat{\mathbf{a}}) = \mathbf{a}$, *i.e.,* an extraction of the vector part of the quaternion. These properties are used extensively in transforming quantities in the $\mathbb{R}^3$ space in the equations of motion Eqs. (22a)–(22c) to quaternions in $\mathbb{R}^4$ and vice versa.

Finally, an extension of the cross product of two vectors $\mathbf{p}$ and $\mathbf{q}$ of $\mathbb{R}^3$ into the set $\mathbb{H}$ is defined by considering the pure quaternion made out of the vector part of the product of the

two associated pure quaternions $\hat{\mathbf{p}} = 0 + \mathbf{p}$ and $\hat{\mathbf{q}} = 0 + \mathbf{q}$:

$$\widehat{\mathbf{p} \times \mathbf{q}} = \hat{\mathbf{p}} \times \hat{\mathbf{q}} = \widehat{\text{vec}(\hat{\mathbf{p}}\,\hat{\mathbf{q}})}. \tag{29}$$

3.2 Rotations written with quaternions

Quaternions represent an alternative to using classical Euler parameters to describe finite rotations [38]. The set of unit quaternions, *i.e.,* quaternions with unit norm $|\hat{\mathbf{q}}| = \hat{\mathbf{q}} \cdot \hat{\mathbf{q}} = 1$, forms a (multiplicative) subgroup of the quaternion group that is able to represent rotation in 3D Euclidean space. The use of quaternions to describe rotations is particularly convenient due to the ability to describe the rotations with only 4 parameters (versus the 9 components of a classical rotation matrix) while remaining exactly equivalent to it. This ability can lead to greater computational efficiency in computing the rotations, since far fewer operations (multiplications and additions) are needed [53].

A general unit quaternion can be written under the following form:

$$\hat{\mathbf{q}} = \cos\left(\frac{\theta}{2}\right) + \sin\left(\frac{\theta}{2}\right)\mathbf{n} = \begin{bmatrix} q_0 & q_1 & q_2 & q_3 \end{bmatrix}^{\mathrm{T}}, \tag{30}$$

where $\mathbf{n}$ is a unit vector. As Eq. (30) represents a *unit* quaternion, a unity constraint tied to $\hat{\mathbf{q}}$ is introduced, since the four components of $\hat{\mathbf{q}}$ are not independent. The unit quaternion can be used to represent a rotation of angle θ around the axis oriented by the vector $\mathbf{n}$. With $\hat{\mathbf{q}}$ defined in Eq. (30), the rotation operation $\mathbf{R}$ to rotate a vector $\mathbf{p}$ into the vector $\mathbf{p}_r$ such that $\mathbf{p}_r = \mathbf{R}\mathbf{p}$ is rewritten in quaternion algebra as:

$$\hat{\mathbf{p}}_r = \hat{\mathbf{q}}\,\hat{\mathbf{p}}\,\hat{\mathbf{q}}^*. \tag{31}$$

A key observation is made at this point: if $\hat{\mathbf{p}}$ is a pure quaternion ($p_0 = 0$) and $\hat{\mathbf{q}}$ a unit quaternion, then $\hat{\mathbf{p}}_r$ is also a pure quaternion and $\text{vec}(\hat{\mathbf{p}}_r) = \mathbf{p}_r$ is the rotated vector beginning from $\mathbf{p} = \text{vec}(\hat{\mathbf{p}})$. This observation becomes useful in the next section when the variables defined as vectors in Sect. 2 are rewritten as pure quaternions in the governing equations.

Using the same logic, an opposite rotation to rotate $\mathbf{p}_r$ back into $\mathbf{p}$, or $\mathbf{p} = \mathbf{R}^{\mathrm{T}}\mathbf{p}_r$, is written in quaternion algebra as:

$$\hat{\mathbf{p}} = \hat{\mathbf{q}}^*\,\hat{\mathbf{p}}_r\,\hat{\mathbf{q}}. \tag{32}$$

The rotation operations in quaternion formulation as defined in Eqs. (31) and (32) can then be rewritten as matrix multiplications in the form:

$$\hat{\mathbf{p}}_r = \hat{\mathbf{q}}\,\hat{\mathbf{p}}\,\hat{\mathbf{q}}^* = \underbrace{\Phi_R(\hat{\mathbf{q}}^*)\Phi_L(\hat{\mathbf{q}})}_{\mathbf{R}}\hat{\mathbf{p}}, \tag{33a}$$

$$\hat{\mathbf{p}} = \hat{\mathbf{q}}^*\,\hat{\mathbf{p}}_r\,\hat{\mathbf{q}} = \underbrace{\Phi_R(\hat{\mathbf{q}})\Phi_L(\hat{\mathbf{q}}^*)}_{\mathbf{R}^T}\hat{\mathbf{p}}_r. \tag{33b}$$

Based on the 4 components of the unit quaternion $\hat{\mathbf{q}}$ (Eq. (30)) and using the operations $\Phi_L\left(\hat{\mathbf{q}}\right)$ and $\Phi_R\left(\hat{\mathbf{q}}^*\right)$, it is shown in [53] that the equivalent 9 components of $\mathbf{R}$ as a 3D rotation matrix can be written as:

$$\mathbf{R} = \mathbf{R}_{\hat{\mathbf{q}}} = \begin{bmatrix} q_0^2 + q_1^2 - q_2^2 - q_3^2 & 2\left(-q_0 q_3 + q_1 q_2\right) & 2\left(q_0 q_2 + q_1 q_3\right) \\ 2\left(q_0 q_3 + q_2 q_1\right) & q_0^2 - q_1^2 + q_2^2 - q_3^2 & 2\left(-q_0 q_1 + q_2 q_3\right) \\ 2\left(-q_0 q_2 + q_3 q_1\right) & 2\left(q_0 q_1 + q_3 q_2\right) & q_0^2 - q_1^2 - q_2^2 + q_3^2 \end{bmatrix}, \tag{34}$$

which underscores the storage efficiency of the 4-component quaternion (Eq. (30)) by comparison.

3.3 Beam equations rewritten with quaternions

In this section, the principle of virtual work, derived in the previous section, is rewritten using unit quaternions to represent rotations. In what follows, all vector quantities (belonging to $\mathbb{R}^3$) defined in Sect. 2 are replaced with their pure quaternion counterparts using the canonical injection from $\mathbb{R}^3$ to $\mathbb{H}$. For example, the strain vector $\boldsymbol{\Gamma}$ is replaced with the pure quaternion $\hat{\boldsymbol{\Gamma}}$, defined as $\hat{\boldsymbol{\Gamma}} = \begin{bmatrix} 0 & \Gamma_x & \Gamma_y & \Gamma_z \end{bmatrix}^{\mathrm{T}}$.

The 3D equations of motion obtained in this section can, furthermore, be reduced to the case of a 2D beam problem (inplane motion) by restricting the appropriate degrees of freedom. The 2D equations of motion based on the quaternion parametrization are derived in A.

3.3.1 Strain measure, variation, and constitutive law written with quaternions

Using a unit quaternion $\hat{\mathbf{q}}$ to represent the rotation operation as shown in Eqs. (31), (32), and (33a)–(33b), the strains $\hat{\boldsymbol{\Gamma}}$ and curvatures $\hat{\mathbf{K}}$ are written in the form of pure quaternions as:

$$\hat{\boldsymbol{\Gamma}} = \hat{\mathbf{q}}^* \hat{\mathbf{x}}_0' \hat{\mathbf{q}} - \hat{\boldsymbol{\Gamma}}_0, \tag{35a}$$

$$\hat{\mathbf{K}} = 2\hat{\mathbf{q}}^* \hat{\mathbf{q}}' - \hat{\mathbf{K}}_0. \tag{35b}$$

Taking the variation of these expressions leads to:

$$\delta\hat{\boldsymbol{\Gamma}} = 2(\hat{\boldsymbol{\Gamma}} + \hat{\boldsymbol{\Gamma}}_0)\hat{\mathbf{q}}^* \delta\hat{\mathbf{q}} + \hat{\mathbf{q}}^* \delta\hat{\mathbf{x}}_0' \hat{\mathbf{q}}, \tag{36a}$$

$$\delta\hat{\mathbf{K}} = 2\delta\hat{\mathbf{q}}^* \hat{\mathbf{q}}' + 2\hat{\mathbf{q}}^* \delta\hat{\mathbf{q}}' = \hat{\mathbf{q}}^* (2\delta\hat{\mathbf{q}}\hat{\mathbf{q}}^*)' \hat{\mathbf{q}}. \tag{36b}$$

Comparing Eqs. (36a)–(36b) to the expressions of the variations computed in Sect. 2.4 (using a rotation matrix $\mathbf{R}$), the relation between the variation of the angles $\delta\hat{\boldsymbol{\Theta}}$ (seen as a pure quaternion) and the variation of the unit quaternion $\delta\hat{\mathbf{q}}$ is identified as (see also [1]):

$$\delta\hat{\boldsymbol{\Theta}} = 2\hat{\mathbf{q}}^* \delta\hat{\mathbf{q}}, \tag{37}$$

or equivalently in the global frame (recall that $\delta\boldsymbol{\theta} = \mathbf{R}\delta\boldsymbol{\Theta}$):

$$\delta\hat{\boldsymbol{\theta}} = \hat{\mathbf{q}}\delta\hat{\boldsymbol{\Theta}}\hat{\mathbf{q}}^* = 2\delta\hat{\mathbf{q}}\hat{\mathbf{q}}^*. \tag{38}$$

The expression for $\delta\hat{\boldsymbol{\Theta}}'$ written in terms of quaternions is then derived as:

$$\delta\hat{\boldsymbol{\Theta}}' = 2(\hat{\mathbf{q}}^*)' \delta\hat{\mathbf{q}} + 2\hat{\mathbf{q}}^* \delta\hat{\mathbf{q}}'. \tag{39}$$

A formal relation between the variations using rotation matrices and the variations using unit quaternions is then found to be:

$$\begin{bmatrix} \delta\hat{\mathbf{x}}_0' \\ \delta\hat{\mathbf{x}}_0 \\ \delta\hat{\boldsymbol{\Theta}}' \\ \delta\hat{\boldsymbol{\Theta}} \end{bmatrix} = \begin{bmatrix} 1 & 0 & 0 & 0 \\ 0 & 1 & 0 & 0 \\ 0 & 0 & 2\hat{\mathbf{q}}^* & 2\hat{\mathbf{q}}'^* \\ 0 & 0 & 0 & 2\hat{\mathbf{q}}^* \end{bmatrix} \begin{bmatrix} \delta\hat{\mathbf{x}}_0' \\ \delta\hat{\mathbf{x}}_0 \\ \delta\hat{\mathbf{q}}' \\ \delta\hat{\mathbf{q}} \end{bmatrix}. \tag{40}$$

The constitutive relation Eq. (7) can be rewritten directly in terms of quaternions as:

$$\hat{\mathbf{N}} = \hat{\mathbf{C}}_N \hat{\mathbf{\Gamma}} \quad \text{and} \quad \hat{\mathbf{M}} = \hat{\mathbf{C}}_M \hat{\mathbf{K}}, \tag{41}$$

where the 4×4 diagonal matrices $\hat{\mathbf{C}}_N$ and $\hat{\mathbf{C}}_M$ are given by:

$$\hat{\mathbf{C}}_N = \text{diag}\left(0, \quad EA, \quad k_y GA, \quad k_z GA\right) \quad \text{and} \quad \hat{\mathbf{C}}_M = \text{diag}\left(0, \quad GJ, \quad EI_y, \quad EI_z\right). \tag{42}$$

3.3.2 Principle of virtual work

The principle of virtual work can now be rewritten in terms of quaternion variables. For this, every 3×1 vector of $\mathbb{R}^3$ is replaced with its associated pure quaternion in $\mathbb{H}$. Then, the virtual work of the acceleration forces δW_a (recalling that the rotary inertia of the cross sections is neglected in this study) is rewritten as:

$$\delta W_a = \int_0^L \rho A \ddot{\hat{\mathbf{x}}}_0^{\mathrm{T}} \delta \hat{\mathbf{x}}_0 \mathrm{d}s. \tag{43}$$

The virtual work of the internal forces δW_i is likewise rewritten as:

$$\delta W_i = -\int_0^L \left(\hat{\mathbf{N}}^{\mathrm{T}} \delta \hat{\mathbf{\Gamma}} + \hat{\mathbf{M}}^{\mathrm{T}} \delta \hat{\mathbf{K}}\right) \mathrm{d}s. \tag{44}$$

Finally, the virtual work of the external forces δW_e is rewritten as:

$$\delta W_e = \int_0^L \left(\hat{\mathbf{n}}_e^{\mathrm{T}} \delta \hat{\mathbf{x}}_0 + \hat{\mathbf{m}}_e^{\mathrm{T}} (2\delta \hat{\mathbf{q}} \hat{\mathbf{q}}^*)\right) \mathrm{d}s + \left[\hat{\mathbf{f}}_e^{\mathrm{T}} \delta \hat{\mathbf{x}}_0\right]_0^L + \left[\hat{\mathbf{c}}_e^{\mathrm{T}} (2\delta \hat{\mathbf{q}} \hat{\mathbf{q}}^*)\right]_0^L. \tag{45}$$

In addition to δW_a, δW_i, and δW_e, the unity constraint for a unit quaternion $\hat{\mathbf{q}}$ representing a rotation must be considered, *i.e.*, $\hat{\mathbf{q}} \cdot \hat{\mathbf{q}} - 1 = 0$. For this, a Lagrange multiplier $\mu = \mu(s)$ is introduced with the virtual work of the constraint δW_μ defined as [1, 42]:

$$\delta W_\mu = \int_0^L \delta \left(\mu \left(\hat{\mathbf{q}} \cdot \hat{\mathbf{q}} - 1\right)\right) \mathrm{d}s = \int_0^L \left(\left(\hat{\mathbf{q}} \cdot \hat{\mathbf{q}} - 1\right) \delta\mu + 2\mu \hat{\mathbf{q}}^{\mathrm{T}} \delta \hat{\mathbf{q}}\right) \mathrm{d}s. \tag{46}$$

The principle of virtual work then takes the form [37]:

$$\delta W_a - \delta W_i - \delta W_e + \delta W_\mu = 0, \quad \forall \delta \mathbf{x}, \delta\mu. \tag{47}$$

In order to derive an explicit expression for the principle of virtual work as in Sect. 2.5, the vector quantities are replaced with their pure quaternion counterparts in Eq. (24), the rotation operator $\mathbf{Rx}$ is replaced with its quaternion counterpart $\hat{\mathbf{q}}\hat{\mathbf{x}}\hat{\mathbf{q}}^*$ and the relation in Eq. (40) is introduced along with the virtual work of the constraint. Combining everything, the following expression is derived:

$$\int_0^L \begin{bmatrix} \hat{\mathbf{q}}\hat{\mathbf{N}}\hat{\mathbf{q}}^* \\ \rho A \ddot{\hat{\mathbf{x}}}_0 - \hat{\mathbf{n}}_e \\ \hat{\mathbf{M}} \\ \left(\hat{\mathbf{N}} \times (\hat{\mathbf{\Gamma}} + \hat{\mathbf{\Gamma}}_0) + \hat{\mathbf{M}} \times \hat{\mathbf{K}} - \hat{\mathbf{q}}^* \hat{\mathbf{m}}_e \hat{\mathbf{q}}\right) \end{bmatrix}^T \begin{bmatrix} 1 & 0 & 0 & 0 \\ 0 & 1 & 0 & 0 \\ 0 & 0 & 2\hat{\mathbf{q}}^* & 2\hat{\mathbf{q}}'^* \\ 0 & 0 & 0 & 2\hat{\mathbf{q}}^* \end{bmatrix} \begin{bmatrix} \delta \hat{\mathbf{x}}_0' \\ \delta \hat{\mathbf{x}}_0 \\ \delta \hat{\mathbf{q}}' \\ \delta \hat{\mathbf{q}} \end{bmatrix} \mathrm{d}s$$

$$+\int_0^L \left(\left(\hat{\mathbf{q}}\cdot\hat{\mathbf{q}}-1\right)\delta\mu+2\mu\hat{\mathbf{q}}^{\mathrm{T}}\delta\hat{\mathbf{q}}\right)\mathrm{d}s=0, \tag{48}$$

which can be rewritten as:

$$\int_0^L \begin{bmatrix} \hat{\mathbf{q}}\hat{\mathbf{N}}\hat{\mathbf{q}}^* \\ \rho A\ddot{\hat{\mathbf{x}}}_0-\hat{\mathbf{n}}_e \\ 2\hat{\mathbf{q}}\hat{\mathbf{M}} \\ 2\hat{\mathbf{q}}'\hat{\mathbf{M}}+2\hat{\mathbf{q}}\left(\hat{\mathbf{N}}\times(\hat{\mathbf{\Gamma}}+\hat{\mathbf{\Gamma}}_0)+(\hat{\mathbf{M}}\times\hat{\mathbf{K}})\right)+2\mu\hat{\mathbf{q}}-2\hat{\mathbf{m}}_e\hat{\mathbf{q}} \\ \hat{\mathbf{q}}\cdot\hat{\mathbf{q}}-1 \end{bmatrix}^T \begin{bmatrix} \delta\hat{\mathbf{x}}_0' \\ \delta\hat{\mathbf{x}}_0 \\ \delta\hat{\mathbf{q}}' \\ \delta\hat{\mathbf{q}} \\ \delta\mu \end{bmatrix} \mathrm{d}s=0. \tag{49}$$

Finally, since $\hat{\mathbf{x}}_0$, $\hat{\mathbf{N}}$ and $\hat{\mathbf{n}}_e$ are pure quaternions, they can be reduced by discarding their scalar parts so that Eq. (49) is rewritten in terms of the 3×1 vectors $\mathbf{x}_0$ (and its derivative $\mathbf{x}_0'$ and their respective variations), $\mathbf{N}$ and $\mathbf{n}_e$ as:

$$\int_0^L \begin{bmatrix} \mathbf{R}_{\hat{\mathbf{q}}}\mathbf{N} \\ \rho A\ddot{\mathbf{x}}_0-\mathbf{n}_e \\ 2\hat{\mathbf{q}}\hat{\mathbf{M}} \\ 2\hat{\mathbf{q}}'\hat{\mathbf{M}}+2\hat{\mathbf{q}}\left(\hat{\mathbf{N}}\times(\hat{\mathbf{\Gamma}}+\hat{\mathbf{\Gamma}}_0)+(\hat{\mathbf{M}}\times\hat{\mathbf{K}})\right)+2\mu\hat{\mathbf{q}}-2\hat{\mathbf{m}}_e\hat{\mathbf{q}} \\ \hat{\mathbf{q}}\cdot\hat{\mathbf{q}}-1 \end{bmatrix}^T \begin{bmatrix} \delta\mathbf{x}_0' \\ \delta\mathbf{x}_0 \\ \delta\hat{\mathbf{q}}' \\ \delta\hat{\mathbf{q}} \\ \delta\mu \end{bmatrix} \mathrm{d}s=0, \tag{50}$$

where $\mathbf{R}_{\hat{\mathbf{q}}}$ is the rotation matrix expressed in terms of the components of the quaternion $\hat{\mathbf{q}}$ as given in Eq. (34), verifying the property $\mathbf{R}_{\hat{\mathbf{q}}}\mathbf{N}=\mathrm{vec}(\hat{\mathbf{q}}\hat{\mathbf{N}}\hat{\mathbf{q}}^*)$.

4 Discretization into finite elements and resolution procedure

Next, in this section, discretization of the geometrically exact beam problem with unit quaternion description of the rotations based on the finite-element (FE) method is presented. In addition, some important details related to the solving procedure based on the Asymptotic Numerical Method (ANM) are described.

4.1 Definition of the FE interpolation

In general, quaternions/rotations, which are multiplicative quantities, cannot be properly interpolated additively [7]. Rather than using more complex interpolations (*e.g.,* interpolation on the special Euclidean group SE(3) that respects the multiplicativity of the rotations [24, 33]), we choose instead to rely on a quadratic interpolation for its ease of implementation. This can lead to small errors due to loss of objectivity with polynomial interpolations [7], but the errors are minimized by using a sufficiently refined mesh.

The beam is discretized into N_e finite elements of length L_e with two boundary nodes and one internal node equidistant from the two boundary nodes (recall the quadratic interpolation). At each node, there are 8 degrees of freedom (dof) corresponding to the displacement of the centerline $\mathbf{x}_0$ (3 dof), the quaternion used to describe the rotation of the cross section $\hat{\mathbf{q}}$ (4 dof) and the Lagrange multiplier μ (1 dof). For a given element, the interpolation of the various fields is written as:

$$\begin{bmatrix} \mathbf{x}_0^e(s,t) \\ \hat{\mathbf{q}}^e(s,t) \\ \mu^e(s,t) \end{bmatrix} = \mathbf{P}(s)\mathbf{z}^e(t), \quad \forall s\in[0\ L_e], \tag{51}$$

where $\mathbf{P}(s)$ is the interpolation matrix (of size 8×24) and $\mathbf{z}^e(t)$ is the vector of element dof (of size 24×1) defined as:

$$\mathbf{z}^e = [\underbrace{\mathbf{x}_{0,1}^{\mathrm{T}} \quad \hat{\mathbf{q}}_1^{\mathrm{T}} \quad \mu_1}_{\text{node 1}} \quad \underbrace{\mathbf{x}_{0,2}^{\mathrm{T}} \quad \hat{\mathbf{q}}_2^{\mathrm{T}} \quad \mu_2}_{\text{node 2}} \quad \underbrace{\mathbf{x}_{0,3}^{\mathrm{T}} \quad \hat{\mathbf{q}}_3^{\mathrm{T}} \quad \mu_3}_{\text{node 3}}]^{\mathrm{T}}. \tag{52}$$

The interpolation matrix $\mathbf{P}(s)$ can be conveniently written as:

$$\mathbf{P}(s) = \begin{bmatrix} N_1(s)\mathbf{I}_8, & N_2(s)\mathbf{I}_8, & N_3(s)\mathbf{I}_8 \end{bmatrix}, \tag{53}$$

where $\mathbf{I}_8$ represents the 8×8 identity matrix and $N_1,\ N_2,\ N_3$ are the quadratic shape functions, defined over a given element of length L_e as, $\forall s \in [0\ L_e]$:

$$N_1(s) = 2\left(\frac{s}{L^e}\right)^2 - 3\left(\frac{s}{L^e}\right) + 1, \tag{54a}$$

$$N_2(s) = -4\left(\frac{s}{L^e}\right)^2 + 4\left(\frac{s}{L^e}\right), \tag{54b}$$

$$N_3(s) = 2\left(\frac{s}{L^e}\right)^2 - \left(\frac{s}{L^e}\right). \tag{54c}$$

The space derivatives are then defined as:

$$\begin{bmatrix} \mathbf{x}_0^{e\prime}(s,t) \\ \hat{\mathbf{q}}^{e\prime}(s,t) \\ \mu^{e\prime}(s,t) \end{bmatrix} = \mathbf{P}'(s)\mathbf{z}^e(t) = \begin{bmatrix} N_1'(s)\mathbf{I}_8 & N_2'(s)\mathbf{I}_8 & N_3'(s)\mathbf{I}_8 \end{bmatrix} \mathbf{z}^e(t). \tag{55}$$

The variation of the fields (and their derivatives) over a single element can be rewritten in matrix form as:

$$\begin{bmatrix} \delta\mathbf{x}_0^{e\prime} \\ \delta\mathbf{x}_0^{e} \\ \delta\hat{\mathbf{q}}^{e\prime} \\ \delta\hat{\mathbf{q}}^{e} \\ \delta\mu^{e} \end{bmatrix} = \mathbf{Q}(s)\delta\mathbf{z}^e, \tag{56}$$

where $\delta\mathbf{z}^e$ is the variation of the element degrees of freedom, and where the interpolation matrix $\mathbf{Q}(s)$ (of size 15×24) is defined as:

$$\mathbf{Q}(s) = \begin{bmatrix} N_1'\mathbf{I}_3 & \mathbf{0} & \mathbf{0} & N_2'\mathbf{I}_3 & \mathbf{0} & \mathbf{0} & N_3'\mathbf{I}_3 & \mathbf{0} & \mathbf{0} \\ N_1\mathbf{I}_3 & \mathbf{0} & \mathbf{0} & N_2\mathbf{I}_3 & \mathbf{0} & \mathbf{0} & N_3\mathbf{I}_3 & \mathbf{0} & \mathbf{0} \\ \mathbf{0} & N_1'\mathbf{I}_4 & \mathbf{0} & \mathbf{0} & N_2'\mathbf{I}_4 & \mathbf{0} & \mathbf{0} & N_3'\mathbf{I}_4 & \mathbf{0} \\ \mathbf{0} & N_1\mathbf{I}_4 & \mathbf{0} & \mathbf{0} & N_2\mathbf{I}_4 & \mathbf{0} & \mathbf{0} & N_3\mathbf{I}_4 & \mathbf{0} \\ \mathbf{0} & \mathbf{0} & N_1 & \mathbf{0} & \mathbf{0} & N_2 & \mathbf{0} & \mathbf{0} & N_3 \end{bmatrix}, \tag{57}$$

where $\mathbf{I}_n$ represents the $n \times n$ identity matrix.

4.2 Principle of virtual work and elementary equations of motion

Beginning from the expression of the principle of virtual work given in Eq. (50), the elementary fields and the discretization are introduced by transforming the integral over the entire beam length into a sum of integrals over each individual element. Incorporating Eq. (56),

the principle of virtual work given in Eq. (50) is written (for only a single element for the sake of simplicity):

$$(\delta\mathbf{z}^e)^T \int_0^{L_e} \mathbf{Q}(s)^T \left(\begin{bmatrix} \mathbf{0} \\ \rho A \ddot{\mathbf{x}}_0^e \\ \mathbf{0} \\ \mathbf{0} \\ 0 \end{bmatrix} + \begin{bmatrix} \mathbf{R}^e_{\hat{\mathbf{q}}^e} \mathbf{N}^e \\ \mathbf{0} \\ 2\hat{\mathbf{q}}^e \hat{\mathbf{M}}^e \\ 2\hat{\mathbf{q}}^{e\prime} \hat{\mathbf{M}}^e + 2\hat{\mathbf{q}}^e \left(\hat{\mathbf{N}}^e \times (\hat{\mathbf{\Gamma}}^e + \hat{\mathbf{\Gamma}}_0^{\ e}) + (\hat{\mathbf{M}}^e \times \hat{\mathbf{K}}^e) \right) \\ 0 \end{bmatrix} + \begin{bmatrix} \mathbf{0} \\ -\mathbf{n}_e^e \\ \mathbf{0} \\ -2\hat{\mathbf{m}}_e^e \hat{\mathbf{q}}^e \\ 0 \end{bmatrix} + \begin{bmatrix} \mathbf{0} \\ \mathbf{0} \\ \mathbf{0} \\ 2\mu^e \hat{\mathbf{q}}^e \\ \hat{\mathbf{q}}^e \cdot \hat{\mathbf{q}}^e - 1 \end{bmatrix} \right) \mathrm{d}s = 0. \tag{58}$$

With the previous relation holding for any $\delta\mathbf{z}^e$, the equation of motion for a single element can be written as:

$$\mathbf{F}_a^e + \mathbf{F}_i^e + \mathbf{F}_\mu^e = \mathbf{F}_e^e, \tag{59}$$

where $\mathbf{F}_a^e$, $\mathbf{F}_i^e$, $\mathbf{F}_\mu^e$, and $\mathbf{F}_e^e$ are, respectively, the inertial forces, the internal forces, the constraint forces, and the external forces acting over the element and defined hereafter.

The inertial force vector $\mathbf{F}_a^e$ is defined as:

$$\begin{aligned} \mathbf{F}_a^e &= \int_0^{L_e} \mathbf{Q}(s)^T \begin{bmatrix} \mathbf{0} \\ \rho A \ddot{\mathbf{x}}_0^e \\ \mathbf{0} \\ \mathbf{0} \\ 0 \end{bmatrix} \mathrm{d}s = \left(\int_0^{L_e} \rho A \mathbf{Q}(s)^T \begin{bmatrix} 0 & 0 & 0 & 0 & 0 \\ 0 & \mathbf{I}_3 & 0 & 0 & 0 \\ 0 & 0 & 0 & 0 & 0 \\ 0 & 0 & 0 & 0 & 0 \\ 0 & 0 & 0 & 0 & 0 \end{bmatrix} \mathbf{Q}(s) \mathrm{d}s \right) \ddot{\mathbf{z}}^e \\ &= \mathbb{M}^e \ddot{\mathbf{z}}^e, \end{aligned} \tag{60}$$

where $\mathbb{M}^e$ is the mass matrix of the system (of size 24×24), which is found after (exact) integration over the element to be:

$$\mathbb{M}^e = \frac{\rho A L^e}{30} \begin{bmatrix} 4\mathbf{I}_3 & \mathbf{0} & \mathbf{0} & 2\mathbf{I}_3 & \mathbf{0} & \mathbf{0} & -\mathbf{I}_3 & \mathbf{0} & \mathbf{0} \\ \mathbf{0} & \mathbf{0} & \mathbf{0} & \mathbf{0} & \mathbf{0} & \mathbf{0} & \mathbf{0} & \mathbf{0} & \mathbf{0} \\ \mathbf{0} & \mathbf{0} & 0 & \mathbf{0} & \mathbf{0} & 0 & \mathbf{0} & \mathbf{0} & 0 \\ 2\mathbf{I}_3 & \mathbf{0} & \mathbf{0} & 16\mathbf{I}_3 & \mathbf{0} & \mathbf{0} & 2\mathbf{I}_3 & \mathbf{0} & \mathbf{0} \\ \mathbf{0} & \mathbf{0} & \mathbf{0} & \mathbf{0} & \mathbf{0} & \mathbf{0} & \mathbf{0} & \mathbf{0} & \mathbf{0} \\ \mathbf{0} & \mathbf{0} & 0 & \mathbf{0} & \mathbf{0} & 0 & \mathbf{0} & \mathbf{0} & 0 \\ -\mathbf{I}_3 & \mathbf{0} & \mathbf{0} & 2\mathbf{I}_3 & \mathbf{0} & \mathbf{0} & 4\mathbf{I}_3 & \mathbf{0} & \mathbf{0} \\ \mathbf{0} & \mathbf{0} & \mathbf{0} & \mathbf{0} & \mathbf{0} & \mathbf{0} & \mathbf{0} & \mathbf{0} & \mathbf{0} \\ \mathbf{0} & \mathbf{0} & 0 & \mathbf{0} & \mathbf{0} & 0 & \mathbf{0} & \mathbf{0} & 0 \end{bmatrix}. \tag{61}$$

Recall that the Lagrange multiplier μ is only a mathematical parameter introduced to impose the unity constraint tied to $\hat{\mathbf{q}}$ and therefore contributes no mass. Because of the introduction of μ, the system is a differential-algebraic system of equations (DAE) and therefore has a singular mass matrix. In addition, the rotational inertia of the cross sections is neglected, an additional singularity is created (there are empty rows and columns in the mass matrix at positions associated to quaternions degree of freedom).

Next, the internal force vector $\mathbf{F}_i^e$, the constraint force vector $\mathbf{F}_\mu^e$, and the external force vector $\mathbf{F}_e^e$ are written under a common form $\mathbf{F}_\alpha^e$ (with $\alpha = i, e, \mu$) as:

$$\mathbf{F}_\alpha^e = \int_0^{L_e} \mathbf{Q}(s)^T \mathbf{f}_\alpha^e(\mathbf{z}^e) \mathrm{d}s, \tag{62}$$

where:

$$\begin{aligned}
\mathbf{f}_i^e(\mathbf{z}^e) &= \begin{bmatrix} \mathbf{R}_{\hat{\mathbf{q}}^e}^e \mathbf{N}^e \\ \mathbf{0} \\ 2\hat{\mathbf{q}}^e \hat{\mathbf{M}}^e \\ 2\hat{\mathbf{q}}^{e\prime} \hat{\mathbf{M}}^e + 2\hat{\mathbf{q}}^e \left(\hat{\mathbf{N}}^e \times (\hat{\mathbf{\Gamma}}^e + \hat{\mathbf{\Gamma}}_0^{\ e}) + (\hat{\mathbf{M}}^e \times \hat{\mathbf{K}}^e) \right) \\ 0 \end{bmatrix}, \\
\mathbf{f}_e^e(\mathbf{z}^e) &= \begin{bmatrix} \mathbf{0} \\ \mathbf{n}_e^e \\ \mathbf{0} \\ 2\hat{\mathbf{m}}_e^e \hat{\mathbf{q}}^e \\ 0 \end{bmatrix}, \quad \mathbf{f}_\mu^e(\mathbf{z}^e) = \begin{bmatrix} \mathbf{0} \\ \mathbf{0} \\ \mathbf{0} \\ 2\mu^e \hat{\mathbf{q}}^e \\ \hat{\mathbf{q}}^e \cdot \hat{\mathbf{q}}^e - 1 \end{bmatrix}.
\end{aligned} \tag{63}$$

In order to avoid the effect known as shear locking associated with Timoshenko beam models, the integral in Eq. (62) is evaluated with (two-point) reduced Gaussian integration (the two points stemming from the use of quadratic shape functions) [54]. For a 3-node element of length L_e, the Gauss points are located at abscissa $s_1 = \frac{L^e}{2}\left(1 - \frac{1}{\sqrt{3}}\right)$ and $s_2 = \frac{L^e}{2}\left(1 + \frac{1}{\sqrt{3}}\right)$. In this case, $\mathbf{F}_\alpha^e$ is computed as:

$$\mathbf{F}_\alpha^e = \int_0^{L^e} \mathbf{Q}^{\mathrm{T}} \mathbf{f}_\alpha^e(\mathbf{z}^e) \mathrm{d}s \approx \frac{L^e}{2} \left[\mathbf{Q}^{\mathrm{T}}(s_1) \mathbf{f}_\alpha^e(\mathbf{z}^e(s_1)) + \mathbf{Q}^{\mathrm{T}}(s_2) \mathbf{f}_\alpha^e(\mathbf{z}^e(s_2)) \right]. \tag{64}$$

Having determined the expressions for the elementary matrices and force vectors, the system of equations for the full structure can now be assembled. We introduce the vector $\mathbf{z}$, of size $8N_n \times 1$, which gathers all nodal degrees of freedom of the structure:

$$\mathbf{z} = \begin{bmatrix} \mathbf{x}_{0,1}^{\mathrm{T}} & \hat{\mathbf{q}}_1^{\mathrm{T}} & \mu_1 & \mathbf{x}_{0,2}^{\mathrm{T}} & \hat{\mathbf{q}}_2^{\mathrm{T}} & \mu_2 & \dots & \mathbf{x}_{0,N_n}^{\mathrm{T}} & \hat{\mathbf{q}}_{N_n}^{\mathrm{T}} & \mu_{N_n} \end{bmatrix}^{\mathrm{T}}. \tag{65}$$

After assembly of the various elementary force vectors, the equations of motion for the discretized beam take the following general form, where a Rayleigh damping has been a posteriori introduced:

$$\mathbb{M}\ddot{\mathbf{z}} + \mathbb{D}\dot{\mathbf{z}} + \mathbf{F}_{\mathrm{int}}(\mathbf{z}) = \mathbf{F}_{\mathrm{ext}}, \tag{66}$$

where $\mathbb{M}$ is the mass matrix of the full system (of size $8N_n \times 8N_n$ and denoted with double bars so as not to be confused with the internal moment vector), $\mathbb{D}$ is the linear Rayleigh damping matrix, $\mathbf{F}_{\mathrm{int}} = \mathbf{F}_i + \mathbf{F}_\mu$ is the internal force vector (taking into account the constraint forces), and $\mathbf{F}_{\mathrm{ext}}$ is the external forces vector.

4.3 Quadratic recast of the 3D system

The harmonic balance method–asymptotic numerical method numerical strategy for continuation of periodic solutions, already implemented in the software MANLAB, is used here in

the same way as in the 2D case of [2]. This strategy enables direct computation of the forced response of Eq. (66) under periodic excitation ($\mathbf{F}_{\text{ext}}(t)$ is time periodic) or the nonlinear modes (the solution to the underlying free conservative system of Eq. (66)).

In the MANLAB formalism, the input governing equation of the dynamical problem should be rewritten in the form of a differential-algebraic system of equations (DAE) with at most quadratic nonlinearities [55, 56]. Once the quadratic DAE is defined, the harmonic balance method is applied, leading to a set of algebraic equations depending on a parameter (usually the angular frequency). The asymptotic numerical method is applied to solve the algebraic system [57], leading to solutions in the form of parametrized curves (each variable of the algebraic system and the angular frequency are expressed as a power series of a continuation parameter). The quadratic DAE formalism allows for the ability to deal with a large variety of nonlinearities, provided that the original dynamics can be expressed in the form of a quadratic DAE through a procedure called the quadratic recast [55, 58], a procedure that usually involves the definition of additional variables (called auxiliary variables).

In what follows, the quadratic recast procedure is presented for the geometrically exact beam model. This procedure is rendered straightforward by the polynomial nature of the nonlinearities when written with the present quaternion parametrization. In particular, no transcendental functions such as sine and cosine functions are required, as was the case in [2]. To this end, we introduce auxiliary variables and we proceed to the quadratic recast following a procedure analogous to the one described in [1].

In this case, only the term $\mathbf{F}_{\text{int}} = \mathbf{F}_i + \mathbf{F}_\mu$ contains polynomial expressions of degree greater than two and therefore must be rewritten. To exemplify the procedure, consider only a single element. To begin, the expression of $\mathbf{F}^e_{\text{int}}$ is recalled here explicitly:

$$\mathbf{F}^e_{\text{int}} = \int_0^{L_e} \mathbf{Q}(s)^T \underbrace{\begin{bmatrix} \mathbf{R}^e_{\hat{\mathbf{q}}^e}\mathbf{N}^e \\ \mathbf{0} \\ 2\hat{\mathbf{q}}^e\hat{\mathbf{M}}^e \\ 2\hat{\mathbf{q}}^{e\prime}\hat{\mathbf{M}}^e + 2\hat{\mathbf{q}}^e\left(\hat{\mathbf{N}}^e \times (\hat{\mathbf{\Gamma}}^e + \hat{\mathbf{\Gamma}}_0{}^e) + (\hat{\mathbf{M}}^e \times \hat{\mathbf{K}}^e)\right) + 2\mu^e\hat{\mathbf{q}}^e \\ \hat{\mathbf{q}}^e \cdot \hat{\mathbf{q}}^e - 1 \end{bmatrix}}_{\mathbf{g}^e(\mathbf{z}^e)} \mathrm{d}s \tag{67}$$

$$\approx \frac{L_e}{2}\left[\mathbf{Q}(s_1)^T\mathbf{g}^e(\mathbf{z}^e(s_1)) + \mathbf{Q}(s_2)^T\mathbf{g}^e(\mathbf{z}^e(s_2))\right].$$

In order to render the previous expression quadratic, the expression of the internal force $\mathbf{g}^e(\mathbf{z}^e)$ is rewritten by introducing additional variables called auxiliary variables. At each Gauss point, 17 auxiliary variables (3 vectors and 2 quaternions) are introduced, gathered in the vector $\mathbf{v}^e = \begin{bmatrix}\mathbf{v}_1^{e\mathrm{T}} & \mathbf{v}_2^{e\mathrm{T}} & \mathbf{v}_3^{e\mathrm{T}} & \hat{\mathbf{v}}_4^{e\mathrm{T}} & \hat{\mathbf{v}}_5^{e\mathrm{T}}\end{bmatrix}^{\mathrm{T}}$, defined as (see, *e.g.,* [1]):

$$\begin{cases} \mathbf{v}_1^e = \mathbf{\Gamma}^e = \mathrm{vec}(\hat{\mathbf{\Gamma}}^e) = \mathrm{vec}(\hat{\mathbf{q}}^{e*}\,\hat{\mathbf{x}}_0^{e\prime}\,\hat{\mathbf{q}}^e - \hat{\mathbf{\Gamma}}_0) = \mathrm{vec}(\hat{\mathbf{v}}_4^e\,\hat{\mathbf{q}}^e - \hat{\mathbf{\Gamma}}_0), & \text{(68a)} \\ \mathbf{v}_2^e = \mathbf{K}^e = \mathrm{vec}(\hat{\mathbf{K}}^e) = \mathrm{vec}(2\hat{\mathbf{q}}^{e*}\,\hat{\mathbf{q}}^{e\prime}), & \text{(68b)} \\ \mathbf{v}_3^e = \mathbf{N}^e \times (\mathbf{\Gamma}^e + \mathbf{\Gamma}_0) + \mathbf{M}^e \times \mathbf{K}^e = \mathrm{vec}(\hat{\mathbf{N}}^e \times (\hat{\mathbf{\Gamma}}^e + \hat{\mathbf{\Gamma}}_0{}^e) + \hat{\mathbf{M}}^e \times \hat{\mathbf{K}}^e), & \text{(68c)} \\ \hat{\mathbf{v}}_4^e = \hat{\mathbf{q}}^{e*}\,\hat{\mathbf{x}}_0^{e\prime}, & \text{(68d)} \\ \hat{\mathbf{v}}_5^e = \hat{\mathbf{q}}^e\,\hat{\mathbf{N}}^e. & \text{(68e)} \end{cases}$$

Substituting Eqs. (68a)–(68e) into Eq. (67), the vector $\mathbf{g}^e$ (at a given Gauss point) is recast in quadratic form as:

$$\mathbf{g}^e = \begin{bmatrix} \mathrm{vec}\left(\hat{\mathbf{v}}_5^e \; \hat{\mathbf{q}}^{e*}\right) \\ \mathbf{0} \\ 2\hat{\mathbf{q}}^e \; \left(\hat{\mathbf{C}}_M \hat{\mathbf{v}}_2^e\right) \\ 2\hat{\mathbf{q}}^{e\prime} \; \left(\hat{\mathbf{C}}_M \hat{\mathbf{v}}_2^e\right) + 2\hat{\mathbf{q}}^e \; \hat{\mathbf{v}}_3^e + 2\mu^e \hat{\mathbf{q}}^e \\ \hat{\mathbf{q}}^e \cdot \hat{\mathbf{q}}^e - 1 \end{bmatrix}, \tag{69}$$

where the constitutive relations $\hat{\mathbf{N}}^e = \hat{\mathbf{C}}_N \hat{\mathbf{\Gamma}}^e$ and $\hat{\mathbf{M}}^e = \hat{\mathbf{C}}_M \hat{\mathbf{K}}^e$ have been used in place of $\hat{\mathbf{N}}^e$ and $\hat{\mathbf{M}}^e$, and where $\hat{\mathbf{v}}_3^e$ is the pure quaternion associated to the vector $\mathbf{v}_3^e$.

The final form of the equations of motion for a given element is then obtained by adding the definitions of the auxiliary variables (at the two Gauss points) into the system of equations. This leads to a (first order in time) quadratic DAE of the following form:

$$\dot{\mathbf{z}}_-^e = \mathbf{V}^e, \tag{70a}$$

$$\mathbb{M}^e \dot{\mathbf{V}}_+^e = \mathbf{F}_{\text{ext}}^e - \mathbf{D}^e \mathbf{V}_+^e - \mathbf{F}_{\text{int}}^e, \tag{70b}$$

$$\mathbf{0} = \mathbf{v}_{11}^e - \mathrm{vec}\left(\hat{\mathbf{v}}_{41}^e \; \hat{\mathbf{q}}^e(s_1)\right) + \mathbf{\Gamma}_0, \tag{70c}$$

$$\mathbf{0} = \mathbf{v}_{21}^e - \mathrm{vec}\left(2\hat{\mathbf{q}}^e(s_1)^* \; \hat{\mathbf{q}}^{e\prime}(s_1)\right), \tag{70d}$$

$$\mathbf{0} = \mathbf{v}_{31}^e - \left(\mathbf{C}_N \mathbf{v}_{11}^e\right) \; \mathbf{\Gamma}_0 - \left(\mathbf{C}_N \mathbf{v}_{11}^e\right) \; \mathbf{v}_{11}^e - \left(\mathbf{C}_M \mathbf{v}_{21}^e\right) \; \mathbf{v}_{21}^e, \tag{70e}$$

$$\hat{\mathbf{0}} = \hat{\mathbf{v}}_{41}^e - \hat{\mathbf{q}}^{e*}(s_1) \; \hat{\mathbf{x}}_0^{e\prime}(s_1), \tag{70f}$$

$$\hat{\mathbf{0}} = \hat{\mathbf{v}}_{51}^e - \hat{\mathbf{q}}^e(s_1) \; \left(\hat{\mathbf{C}}_N \hat{\mathbf{v}}_{11}^e\right), \tag{70g}$$

$$\mathbf{0} = \mathbf{v}_{12}^e - \mathrm{vec}\left(\hat{\mathbf{v}}_{42}^e \; \hat{\mathbf{q}}^e(s_2)\right) + \mathbf{\Gamma}_0, \tag{70h}$$

$$\mathbf{0} = \mathbf{v}_{22}^e - \mathrm{vec}\left(2\hat{\mathbf{q}}^e(s_2)^* \; \hat{\mathbf{q}}^{e\prime}(s_2)\right), \tag{70i}$$

$$\mathbf{0} = \mathbf{v}_{32}^e - \left(\mathbf{C}_N \mathbf{v}_{12}^e\right) \; \mathbf{\Gamma}_0 - \left(\mathbf{C}_N \mathbf{v}_{12}^e\right) \; \mathbf{v}_{12}^e - \left(\mathbf{C}_M \mathbf{v}_{22}^e\right) \; \mathbf{v}_{22}^e, \tag{70j}$$

$$\hat{\mathbf{0}} = \hat{\mathbf{v}}_{42}^e - \hat{\mathbf{q}}^{e*}(s_2) \; \hat{\mathbf{x}}_0^{e\prime}(s_2), \tag{70k}$$

$$\hat{\mathbf{0}} = \hat{\mathbf{v}}_{52}^e - \hat{\mathbf{q}}^e(s_2) \; \left(\hat{\mathbf{C}}_N \hat{\mathbf{v}}_{12}^e\right). \tag{70l}$$

For a given element this quadratic DAE contains:

- 24 "displacement" dof (8 per node) contained in $\mathbf{z}^e$;
- 21 "velocity" dof (7 per node, the Lagrange multiplier μ does not have a time derivative) contained in $\mathbf{V}^e$:

$$\mathbf{V}^e = \begin{bmatrix} \mathbf{V}_{\mathbf{x}_{0,1}}^{\mathrm{T}} & \hat{\mathbf{V}}_{\hat{\mathbf{q}}_1}^{\mathrm{T}} & \mathbf{V}_{\mathbf{x}_{0,2}}^{\mathrm{T}} & \hat{\mathbf{V}}_{\hat{\mathbf{q}}_2}^{\mathrm{T}} & \mathbf{V}_{\mathbf{x}_{0,3}}^{\mathrm{T}} & \hat{\mathbf{V}}_{\hat{\mathbf{q}}_3}^{\mathrm{T}} \end{bmatrix}^{\mathrm{T}}; \tag{71}$$

- 34 auxiliary variables (17 per Gauss point) contained in $\mathbf{v}^e$;

so that there is a total of 79 variables per element.

In Eq. (70a), the $\diamond_-$ notation is used to indicate that the rows corresponding to the location of the Lagrange multiplier have been removed in order to match with the dimension

of $\mathbf{V}^e$. Conversely, in Eq. (A.19b), zeros should be added into $\mathbf{V}^e$ and $\dot{\mathbf{V}}^e$ in the locations of the Lagrange multipliers in order to match dimensions with the other quantities. This is indicated by the $\diamond_+$ notation.

4.4 Computation of eigenmodes of the linearized system

The eigenmodes of the structure are computed using the tangent stiffness matrix and the mass matrix of the system. The tangent stiffness can be computed by computing the gradient of the FEM forces relative to the degree of freedom [38].

The computation of the eigenvalues and eigenvectors relies on classical algorithms. In the case of a singular mass matrix, eigenvalues with infinite norm will appear [38], those being linked with the rank deficiency of the mass matrix (i.e., for a mass matrix of size n with rank r, there will be $n - r$ infinite eigenvalues). The modes associates with those infinite eigenvalues are discarded, only the physical modes are kept and used to initialize the continuation of the nonlinear normal modes.

4.5 Scaling of the equations in 3D

Scaling the parameters in order to render the equilibrium equations dimensionless is useful in generalizing any results. The same dimensionless variables as in [2, 59] are introduced here:

$$\bar{\mathbf{u}}_0 = \frac{\mathbf{u}_0}{L}, \quad \bar{\mathbf{x}}_0 = \frac{\mathbf{x}_0}{L}, \quad \bar{s} = \frac{s}{L}, \quad \bar{t} = \frac{t}{L^2}\sqrt{\frac{EI}{\rho A}}, \quad \bar{\omega} = L^2\sqrt{\frac{\rho A}{EI}}\omega, \tag{72a}$$

$$\bar{\mathbf{N}}, \bar{\mathbf{m}}_e = \frac{L^2}{EI}\left(\mathbf{N}, \mathbf{m}_e\right), \quad \bar{\mathbf{M}} = \frac{L}{EI}\mathbf{M}, \quad \bar{\mathbf{n}}_e = \frac{L^3}{EI}\mathbf{n}_e, \tag{72b}$$

where $\bar{\diamond}$ represents a dimensionless quantity and L is a characteristic length of the system, in this case the length of the beam. If these dimensionless parameters are injected into the equations of motion, the system (neglecting the effect of gravity) is found to depend on two parameters, η_y and η_z, which are analogous to the "slenderness" parameter of [2, 59]. For three-dimensional motion, however, there are two transverse polarizations, so that two "slenderness" parameters are considered:

$$\eta_y = \frac{I_y}{AL^2}, \quad \eta_z = \frac{I_z}{AL^2}. \tag{73}$$

As shown in Eqs. (72a)–(72b), however, only one second moment of area I is needed to normalize t, ω, $\mathbf{N}$, $\mathbf{M}$, $\mathbf{n}_e$, and $\mathbf{m}_e$. To be consistent with [2, 59], I_z is used to normalize the parameters. This choice essentially states that, for asymmetrical cross sections, the beam is oriented such that the low bending stiffness due to the slenderness of the beam causes large bending around $\mathbf{u}_z$; for symmetrical or near-symmetrical cross sections, the choice is largely irrelevant). In practice, the dimensionless system is recovered by setting $EI_z = 1$, $EA = 1/\eta_z$, $\rho A = 1$, $\rho I_z = \eta_z$, $\rho I_y = \eta_y$, $L = 1$, $k_z GA = k_z/[2(1+\nu)\eta_z]$, $k_y GA = k_y/[2(1+\nu)\eta_z]$, and $GJ = 1/[2(1+\nu)](1+\eta_y/\eta_z)$. As in [2, 59], the dimensionless 3D beam model based on Timoshenko kinematics also depends on another dimensionless parameter tied to the effect of shearing, one shear parameter μ_y and μ_z for each direction of shearing.

Note that, in what follows, the $\bar{\diamond}$ notation is dropped. For the test cases studied in Sect. 5, the normalization of each system (if applicable) is explicitly stated.

5 Test cases

Next, several test cases are modeled using the FE geometrically exact quaternion-based formulation outlined above in order to validate the simulation strategy with others in the literature and demonstrate its capacity in simulating the nonlinear dynamics of flexible beams. In [2], several test cases were introduced, two of which are taken up again here: the classical cantilever (clamped–free) beam and the clamped–clamped beam. These two structures are selected not only for their simplicity of implementation, but also because they exhibit the two types of dominant nonlinear mechanisms found in flexible beam structures containing geometrical nonlinearities: the axial-bending coupling is the primary nonlinear mechanism of the clamped–clamped beam, while the cantilever beam represents the classic example of the beam in large rotation.

Moreover, these two classical systems are often studied in the literature on nonlinear beam dynamics [28, 36, 60–63]; some of these works are used in what follows as reference simulations in order to validate the quaternion-based model presented in this work. In particular, given that in 3D the beam has two transverse directions orthogonal to the longitudinal direction, we take a special interest in the one-to-one (1:1) internal resonance (IR) phenomenon that is uncovered for beams of (near) symmetrical cross sections. In this case, the beam has two nearly identical eigenfrequencies [64, 65] tied to a transverse bending mode in each of the two transverse directions, leading to a 1:1 coupling between the two nonlinear modes. As will be shown later, the result of the coupling is a combination in phase quadrature of the two transverse polarizations, so that the beam appears to "rotate" between the polarizations. Some examples in the literature can be found for both the cantilever [65] and the clamped–clamped beam [66]. As real manufacturing processes are imperfect and dimensions are traditionally made to certain tolerance levels instead of exact precision, a slightly asymmetrical cross section can be reasonably expected in real-life applications. It is therefore of importance in certain industrial applications, for example in MEMS and NEMS applications [65], to characterize this 1:1 internal resonance in order to make the necessary design choices to avoid or exploit it.

5.1 2D and 3D motions with quaternion formulation

The two test cases under study in this section are simulated using the mesh and simulation parameters collected in Table 1 for elements of equal length (uniform mesh). Moreover, the results of two distinct simulation codes are also compared: the full 3D code described in Sect. 4 and a simplified version of it, based also on a quaternion parametrization of rotations but restricted to inplane (2D) deformations only as described in A. In order to be able to compare the 2D and 3D motions exactly, the same number of elements, nodes, and harmonics retained in the HBM are used in 2D as in 3D; as such, there are far fewer degrees of freedom involved in the 2D computation compared to 3D. In our models, the computational cost is generally tied to the number of degrees of freedom. In 3D, the number of degrees of freedom increases rapidly when more finite elements are used. In general, we aim to minimize the number of elements while preserving a converged solution in order to reduce computation times. The computation time of systems with many degrees of freedom, however, represents a topic of ongoing research (see Sect. 6). This serves to explain why, *e.g.,* for the clamped–clamped beam, only 12 elements are used in this section versus 50 in [2].

In this section, the nonlinear modes, visually depicted as the backbone curves in an amplitude–frequency plot, are the primary focus as in [59]. This is primarily due to the backbone curve being a more efficient way of characterizing the system's nonlinear behavior than several forced-response computations. However, it is fully possible to compute the

Table 1 Mesh and harmonic parameters: number of discrete elements per structure used in numerical simulations, corresponding number FE nodes (+ 1 internal node per element) and harmonics retained in the HBM

Structure	Elements N_e	Nodes $N_n = 2N_e + 1$	Harmonics H
Cantilever	10	21	20
Clamped–clamped	12	25	10

forced response of the quaternion-based model presented in this paper; the method is the same as in [2].

Cantilever The first system under study is the classical cantilever (initially straight) with one end fixed and the other free. With the centerline of the beam aligned with the $\mathbf{u}_x$-direction such that $(\mathbf{u}_x, \mathbf{u}_y, \mathbf{u}_z) = (\mathbf{E}_x, \mathbf{E}_y, \mathbf{E}_z)$ according to Fig. 1, the beam is able to deform in two orthogonal transverse directions, $\mathbf{E}_y$ and $\mathbf{E}_z$. For a beam of perfectly square cross section ($b = h$ where b is the width of the beam (the dimension in the $\mathbf{E}_z$-direction) and h its thickness (the dimension along $\mathbf{E}_y$)), the eigenfrequencies and the motion on each bending mode are identical in each of the transverse polarizations. In order to "create" the 1:1 internal resonance coupling, a small asymmetry or "detuning" [65, 66] is imposed by breaking very slightly the symmetry between b and h. In doing so, the two transverse polarizations become slightly different, in that the eigenfrequencies and mode shapes are separated slightly. Then, when one transverse nonlinear mode is excited, at a certain amplitude of vibration (corresponding to a certain evolution of the oscillation frequency) an intersection or "overlap" between the two modes is induced such that the two resonant frequencies of the nonlinear modes intersect and the second mode (*i.e.,* the twin bending mode in the other transverse direction) is excited in turn.

To visualize this phenomenon, the beam of Vincent *et al.* [65] is used, a beam of length $L = 1$ m and nearly square cross section is modeled ($h = 0.03$ m and $b = 0.03015$ m), leading to a 0.05% detuning in the symmetry of the square cross section. The system is normalized by its characteristic length, here the length of the beam L. The first two (dimensionless) linear resonant frequencies corresponding to the first transverse bending mode in $\mathbf{E}_y$ and $\mathbf{E}_z$ are, respectively, $\omega_1 = 3.5144$ and $\omega_2 = 3.5320$ (a 0.5% detuning between the eigenfrequencies).

Beginning with the first nonlinear mode of the cantilever, the backbone curve of the dimensionless transverse displacement in $\mathbf{E}_y$ at the free end of the cantilever $w(L,t)/L$ (computed as the maximum of the absolute value of the displacement over one period of oscillation) is shown in Fig. 2(a). The same nonlinear behavior as found in [2] is recovered both in 2D and 3D: the well-known hardening trend of the first nonlinear mode of the cantilever beam [2, 36, 59] is recovered. The maximum displacement w/L at the free end of the beam is identical when using both the 2D and 3D quaternion formulations, both of which follow the same pattern as that of Fig. 4(b) in [2] (the backbone of which is inset in Fig. 2(a) for reference; here the internal resonance branches that were shown in [2] are not computed for efficiency). A direct comparison to the backbones of [2] is performed in the next section.

The deformed shape of the cantilever is also traced at very large amplitude and shown in Fig. 3(a) and (b) for both transverse polarizations. The amplitudes along the backbone curves of Fig. 2 at which the deformed shapes are sketched are marked with green circles.

Of greater interest is the second nonlinear mode of the cantilever in 3D as it is on this mode that the 1:1 internal resonance manifests. The second nonlinear mode is shown in Fig. 2(b), where both the transverse displacement in $\mathbf{E}_y$ w/L and the transverse displacement in $\mathbf{E}_z$ v/L are depicted. It is clearly seen that at a certain amplitude in $v(L,t)$, there

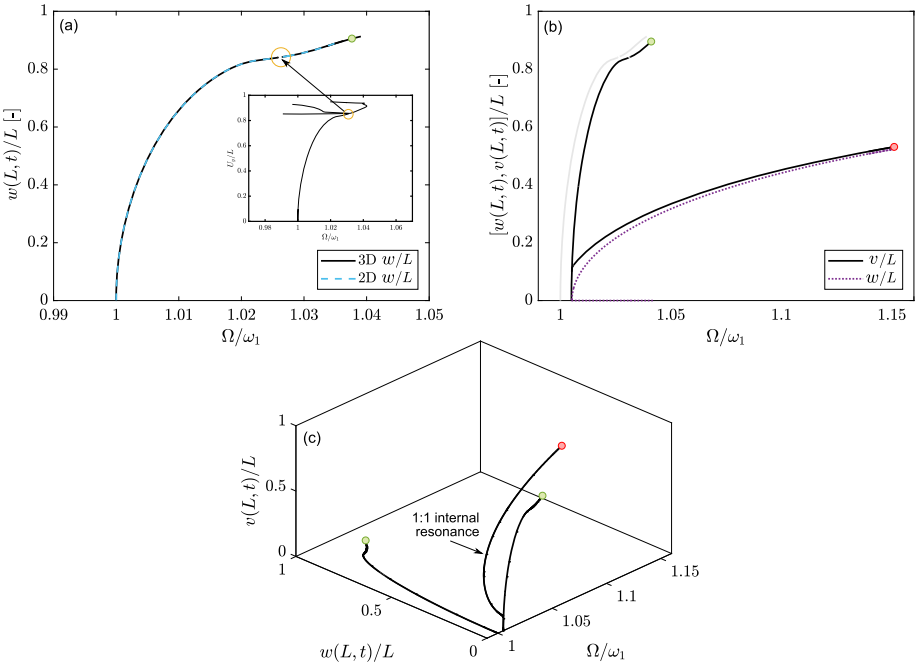

Fig. 2 First nonlinear bending modes of the cantilever beam in the two transverse polarizations, (a) first nonlinear bending-mode polarization: maximum amplitude of $w(L,t)/L$ over one period of oscillation in 2D and 3D, inset: U_y/L backbone of [2] for comparison of the IR at high amplitude, (b) second nonlinear bending-mode polarization: maximum amplitudes of $w(L,t)/L$ and $v(L,t)/L$ over one period of oscillation and 1:1 IR, (c) 3D visualization of the backbone curves (Color figure online)

is a transfer of energy to the first nonlinear bending mode, exemplified by the takeoff of displacement $w(L,t)$ in the other transverse polarization. At this point, the cantilever begins to rotate in an elliptical motion, shown in Fig. 3(c). The amplitude at which Fig. 3(c) is sketched is marked by a red circle in Fig. 2(b). Figure 3 illustrates both the deformed shape in 3D and, in Fig. 3(d)–(f), the projections of the deformed shape in each plane in order to better visualize the motion. In Fig. 2(b), the bifurcation to the elliptic 1:1 internal resonance mode is located at a frequency $\Omega/\omega_1 \simeq 1.005$ and at an amplitude of $v/L \simeq 0.1$, matching the results of [65]. The displacements v/L (in black) and w/L (in purple) are plotted together in Fig. 2(b) to demonstrate the transfer of energy from the $\mathbf{E}_z$-direction mode to the $\mathbf{E}_y$-direction mode. With only a small 0.5% difference between the eigenfrequencies of the two modes, it can be seen in Fig. 3(c) that the beam rotates in almost a perfect circle since the displacements w and v are almost equivalent, especially far from the birth point of the internal resonance branch.

Finally, the backbones are gathered in a 3D plot in Fig. 2(c) following the style of [67]. Each of the bending-mode backbones are fixed in their respective planes, whereas the 1:1 internal resonance branch has components in both w and v. The 3D plot clearly shows the transfer of energy from one polarization to the other.

Clamped–clamped beam Next, the 1:1 internal resonance of the (initially straight) clamped–clamped beam, with both ends of the beam blocked, is investigated following the same procedure as for the cantilever beam. The clamped–clamped beam of Shen *et al.*

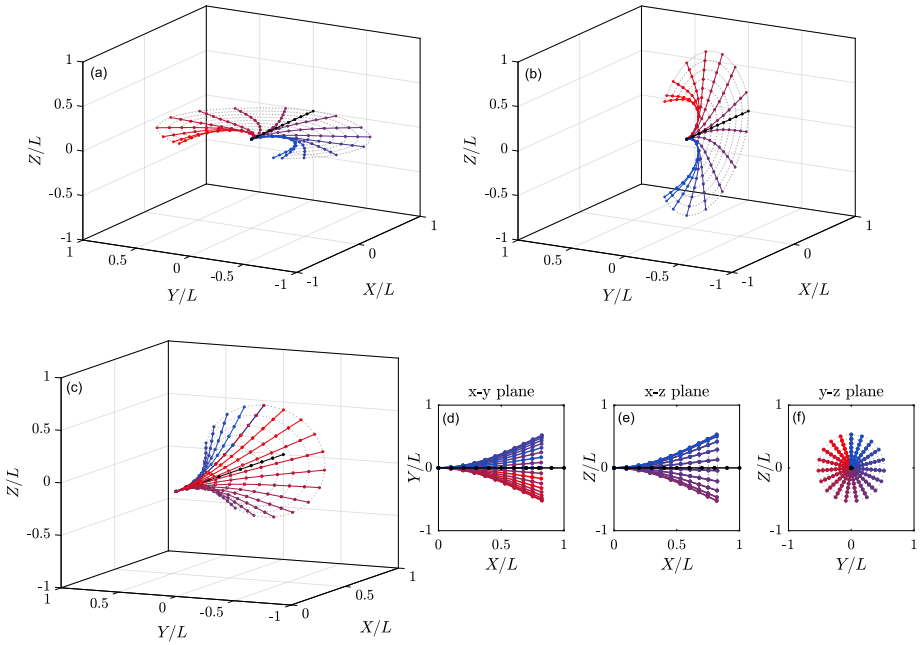

Fig. 3 Deformed shapes of the cantilever beam, (a) high amplitude on the first polarization (green circle in Fig. 2(a)), (b) high amplitude on the second polarization (green circle in Fig. 2(b)), (c)–(f) 1:1 internal resonance between the polarizations and projections onto each plane (red circle in Fig. 2(b)) (Color figure online)

[66] is used ($L = 1$ m, $b = 0.0315$ m, $h = 0.03$) and normalized by L. The dimensions of the beam create a $\sim 5\%$ detuning between the first two (dimensionless) transverse bending eigenfrequencies, which are, in $\mathbf{E}_y$ and $\mathbf{E}_z$, $\omega_1 = 22.2459$ and $\omega_2 = 23.3445$, respectively.

The backbone curves of the clamped–clamped beam are depicted in the same way as for the cantilever beam. We depict w/h and v/h at the midpoint of the beam (the place of maximum displacement). The 1:1 internal resonance of the clamped–clamped beam is uncovered on the first nonlinear mode in contrast to the cantilever system (where it is uncovered on the second). The w/h backbone curve of the first nonlinear bending mode is shown in Fig. 4(a). As with the first nonlinear mode of the cantilever, the main backbone of the first nonlinear mode of the clamped–clamped beam, known to be hardening [2, 60], is found. The second branch depicting the 1:1 internal resonance of the clamped–clamped beam follows much of the same patterns of the cantilever beam: at a certain frequency, there is an energy transfer from the $\mathbf{E}_y$-direction polarization to the $\mathbf{E}_z$-direction where the displacement v/h begins to take off, resulting in the beam rotating along an elliptical trajectory. The deformed shapes of the rotating clamped–clamped beam at high amplitude and on its 1:1 internal resonance branch are shown in Fig. 5(a)–(c), with projections onto each of the planes in Fig. 5(d) and (f). The bifurcation leading to the coupling between the nonlinear modes occurs close to $\Omega/\omega_1 \simeq 1.073$ at an amplitude of $w/h \simeq 0.53$, which matches the reference solution of [66]. In [66], 3D beam finite elements were used in finding the 1:1 internal resonance of the clamped–clamped beam, yet our simplified 1D FE beam model is able to capture the same behavior. This could represent a significant saving in computational cost in simulating a 1D beam model in place of a full 3D beam model.

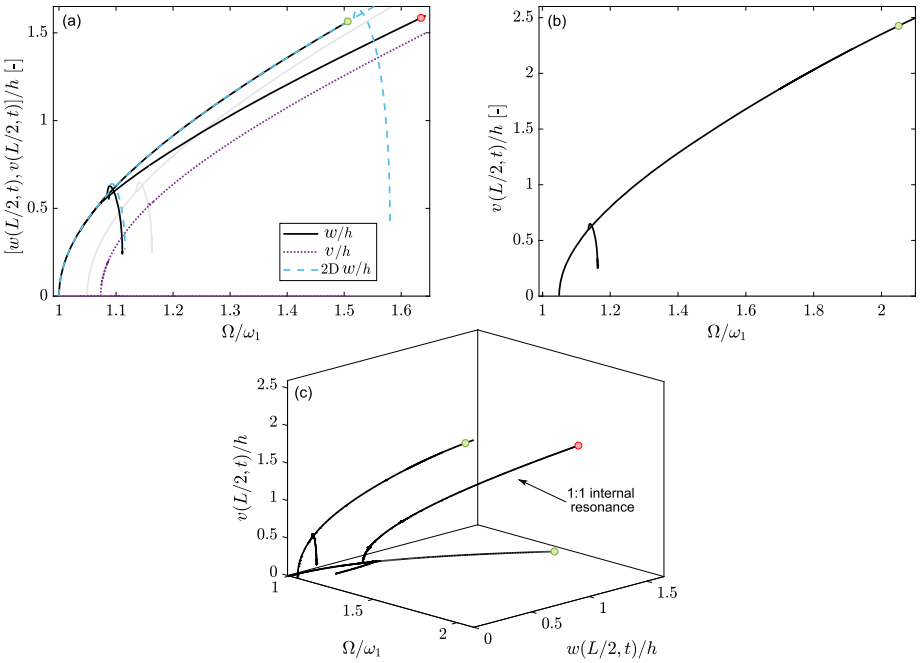

Fig. 4 First nonlinear bending modes of the clamped–clamped beam in the two transverse polarizations, (a) first nonlinear bending-mode polarization: maximum amplitude of $w(L,t)/h$ and $v(L,t)/h$ over one period of oscillation in 2D and 3D and 1:1 IR, (b) second nonlinear bending-mode polarization: maximum amplitude of $v(L,t)/h$ over one period of oscillation, (c) 3D visualization of the backbone curves (Color figure online)

Furthermore, the w/h backbone computed in 3D is compared to the same backbone computed in 2D using the quaternion formulation, which is overlaid as the light blue dashed curve onto Fig. 4(a). The backbone in 2D is in perfect agreement with the backbone in 3D apart from a small shift in the location of the well-known 1:5 internal resonance of the clamped–clamped beam, found also in [2] and in [60]. The shift in the location of the IR is due to small differences in the eigenfrequencies between the 2D and 3D models, something that is discussed in [2]. Nevertheless, the shape of the IR is exactly the same. The backbone curve of the other transverse polarization y/h is shown in Fig. 4(b) in order to visualize the behavior in the second bending polarization. The backbones are also once again combined in a 3D plot in Fig. 4(c) to more easily view the transfer of energy between the bending polarizations.

5.2 2D comparison with rotation-matrix formulation

In the previous section, several references are made to the test cases of [2] using the 2D rotation-matrix formulation. Since the rotation-matrix formulation is validated by both the von Kármán model used in [60] in [2] and the analytical model of Crespo da Silva and Glynn [68–71] at low to moderate amplitudes in [59], a direct comparison between the two 2D formulations (rotation matrices vs. quaternions) serves to validate, if in agreement, the quaternion-based formulation of this paper. Quadratic elements are used for the numerical strategy of the present paper and for the test cases of Sect. 5.1; a direct comparison, however, with the examples of [2] requires that the simulations be performed using the same type of

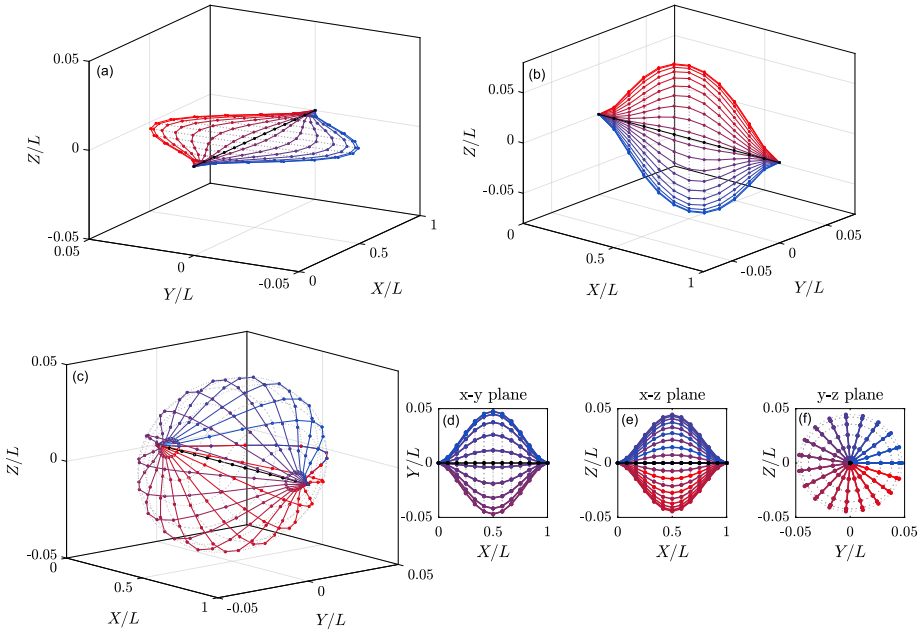

Fig. 5 Deformed shapes of the clamped–clamped beam, (a) high amplitude on the first polarization (green circle in Fig. 4(a)), (b) high amplitude on the second polarization (green circle in Fig. 4(b)), (c)–(f) 1:1 internal resonance between the polarizations and projections onto each plane (red circle in Fig. 4(a)) (Color figure online)

Table 2 Mesh and harmonic parameters: number of discrete elements per structure used in numerical simulations, corresponding number FE nodes and harmonics retained in the HBM

Structure	Elements N_e	Nodes $N_n = N_e + 1$	Harmonics H
Cantilever	20 or 30	21 or 31	20
Clamped–clamped	50	51	10

element (in [2, 59], they are linear). For this reason, the 2D simulations using the quaternion formulation are computed in this section using *linear* elements with the same number of variables as in [2] (number of elements, nodes, and harmonics), summarized in Table 2. The linear elements induce an error when interpolating the quaternion terms due to them being insufficient for accurate interpolation of quaternions, as mentioned in Sect. 4. For this reason, a greater number of *linear* elements should be taken in the quaternion-based formulation to minimize any error.

Cantilever First, we compare the first nonlinear mode of the cantilever beam computed with the quaternion formulation to the cantilever test case of [2]. The backbone curves of the rotation of the cross section θ, the dimensionless transverse displacement at the free end of the cantilever $w(L,t)/L$ and the dimensionless axial displacement $u(L,t)/L$ (computed as the absolute value of the maximum displacement over one period of oscillation) are shown in Fig. 6(a)–(c), respectively. In Fig. 6, three computations are shown: in black is the backbone curve of the rotation-matrix formulation, a direct copy of the backbones of [2], in blue is

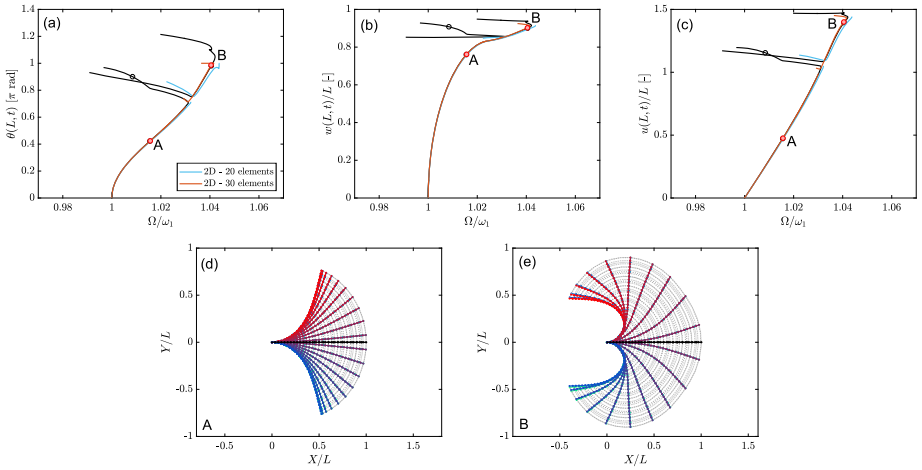

Fig. 6 Comparison of the 2D formulations' first nonlinear mode of the cantilever beam. The backbone curve in black is a reproduction of the one shown in [2] (2D w/ rotation matrices), (a) maximum amplitude of $\theta(L,t)$ over one period of oscillation, (b) maximum amplitude of the transverse displacement $w(L,t)/L$, (c) maximum amplitude of the axial displacement $u(L,t)/L$, (d) deformed shape at point A, representing 20 snapshots over one half-period of motion, overlaid onto the deformed shapes of [2], (e) deformed shape at point B (Color figure online)

the 2D quaternion formulation with 20 elements (the same number as [2]), and in orange is the same 2D quaternion formulation with 30 elements. It is clearly seen from Fig. 6 that the quaternion formulation of this paper yields exactly the same main backbone curve as the rotation-matrix formulation of [2]. This is a good sign, since we know from Sect. 5.1 that the 2D and 3D quaternion formulations likewise yield the same results, thereby indicating that all three formulations are in agreement.

The difference between the blue (2D quat. with 20 elements) and orange (2D quat. with 30 elements) curves in Fig. 6(a)–(c) requires some comment, however. At higher amplitude, beginning around $\theta \simeq 0.5\pi$ rad, the computation with only 20 elements begins to diverge from the computation with 30 elements and the backbone of [2], indicating that the finite-element solution based on the quaternion formulation of the equations of motion is not fully converged with only 20 (linear) elements. This observation is interesting as it demonstrates that, for the same (linear) element, *more elements are required with the quaternion formulation for the solution to be converged*.

Finally, the deformed shapes at moderate (point A) and high (point B) amplitude along the backbone curve computed using the quaternion formulation (with 30 elements) are overlaid onto the deformed shapes computed using the rotation-matrix formulation of [2] in Fig. 6(d) and (e), respectively. Note that since the continuation branches of the two computations are not exactly identical, it is not possible to trace the deformed shape at the exact same point along the two backbone curves. Instead, the closest point of the quaternion computation with 30 elements to the deformed shapes of [2] are selected. It is easily seen in Fig. 6(d) and (e) that the deformed shapes are basically identical. Since the internal resonance offshoots in Fig. 6(a)–(c) are not the same between the 3 computations, the deformed shape on the IR branch is not traced.

Clamped–clamped beam Another comparison is made between the two 2D formulations using the clamped–clamped beam test case of [2]. The clamped–clamped beam represents

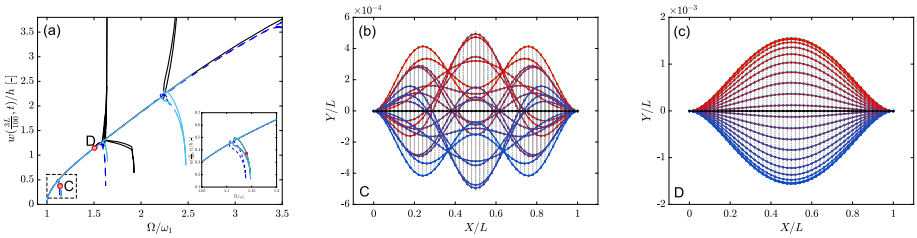

Fig. 7 Comparison of the 2D formulations' first nonlinear mode of the clamped–clamped beam. The backbone curve in black (2D rotation matrices) and of the nonlinear von Kármán in dashed blue are a reproduction of those shown in [2], (a) maximum amplitude of $w(\frac{3L}{100}, t)/h$ over one period of oscillation, (b) deformed shape at point C, representing 20 snapshots over one half-period of motion, overlaid onto the deformed shapes of [2], (e) deformed shape at point D (Color figure online)

an interesting test case beyond the reasons given at the beginning of this section since, as in [2], the geometrically exact model can be validated with the nonlinear von Kármán model. To this end, the simulation of [2] is carried out using the 2D quaternion formulation and the results are shown in Fig. 7. The backbone curve of the first nonlinear mode of the clamped–clamped beam is computed as the maximum transverse displacement over one period of oscillation at the node located at $s = \frac{3L}{100}$ on the beam (normalized by the thickness h of the beam) using the quaternion formulation. The quaternion-based backbone curve is overlaid onto a copy of the rotation-matrix backbone curve (taken from [2]) in Fig. 7(a). Additionally, a zoom onto the 1:5 internal resonance is shown in the inset of Fig. 7(a).

First, it can be seen that as with the cantilever test case, the 2D computation with quaternions exactly matches the 2D computation with rotation matrices, with even the zoom onto the 1:5 internal resonance matching nearly exactly (in contrast to the 3D computation, where the 1:5 IR is slightly shifted from the 2D computation). This observation suggests that the two computations (when converged with a sufficient number of elements) are (nearly) identical, with even the eigenvalues being computed identically. As in [2], the other branches of internal resonance are not as similar in shape as the 1:5 internal resonance (point C), but all occur at nearly identical locations. The main backbone curve, however, is nearly identical across all three models until the von Kármán model begins to diverge around a transverse displacement of $\sim w = 2.5h$. Furthermore, since 50 linear finite elements are used in the simulations of Fig. 7, it can be said that with 50 elements, the quaternion computation is sufficiently converged so as to exactly match the results of the rotation-matrix computation.

Finally, the deformed shapes at points C and D along the backbone curve computed with the quaternion formulation are overlaid onto those recopied from [2]. Unlike for the cantilever beam, here the 1:5 IR branch is nearly identical between the 2D quaternion and rotation-matrix formulations, so that the deformed shape [Fig. 7(b)] is nearly identical. This is likewise the case for the higher-amplitude deformed shape, shown in Fig. 7(c).

6 Conclusion

In this paper, an extension of the work of [2] to three dimensions has been presented. In 3D, rather than continuing with the rotation-matrix parametrization of [2], the rotations are parametrized through the use of unit quaternions, 4-dimensional complex numbers that exactly represent the three rotation degrees of freedom about $(\mathbf{E}_x, \mathbf{E}_y, \mathbf{E}_z)$. First, the geometrically exact beam model, discretized into finite elements, is expressed in 3D with quater-

nion parametrization of the rotations based on quaternion algebra. The beam model is then reduced to 2D inplane motions with the simpler equations being written explicitly for a direct comparison to the rotation-matrix formulation. The cantilever beam and the clamped–clamped beam of [2] serve as test cases in order to validate the quaternion formulation with the results of [2] and other works in the literature.

The limitations of this method lay the foundation for future work. First, due to the very large number of degrees of freedom involved in 3D computations, we are limited to a certain extent by the computation time when many nodes and harmonics are included in the simulation. Not only are there more degrees of freedom in 3D compared to plane motions, but the quaternion elements of the quaternion-based formulation mean that more nodes (and therefore degrees of freedom) are involved in the computation. Although the 3D simulations here based on a 1D geometrically exact beam model remain more efficient than full 3D simulations based on 3D beam elements using, *e.g.,* a FE software package, the 3D simulations shown here are limited to structures composed of ~ 15 or fewer elements, unless the number of harmonics kept in the HBM is reduced (which can lead to inaccuracy if the truncation is too stringent). Ongoing research is looking to find ways to increase the computational efficiency of MANLAB, especially when many degrees of freedom are involved.

Finally, future work aims to carry out a full analysis of the computational performance of the 2D quaternion formulation, especially when compared to the 2D rotation-matrix formulation of [2]. Even though it can be said that the two methods "compute the same thing," nevertheless it is still of scientific interest to compare different ways of writing the equations of motion with the aim of improving computational efficiency. A full study comparing the computational efficiency of the two approaches is envisioned to investigate the efficiency of the quaternion formulation in computing the complex dynamics of flexible 1D systems. A method of comparing the computational speeds of the two approaches must be devised, which would take into account (1) the method of carrying out the quadratic recast (since some ways of rewriting the system are more efficient than others, as was discussed in [2]), (2) the initialization time of the system based on the number of degrees of freedom, (3) the number of computed continuation branches, (4) the computation time per branch, *etc*. Future work beyond this can then investigate other ways of parametrizing the rotation terms, *e.g.,* based on Lie groups, and interpolating the rotation field in order to further accelerate the computation time.

Appendix A: Geometrically exact beam equations using quaternions for 2D motion

In this appendix, the process of restricting the beam equations of motion using unit quaternions to represent rotations from 3D to 2D (inplane) motions is introduced. This is of interest as it enables (i) to write explicitly each equation (especially the moment equation), and (ii) to draw a direct comparison with the same model using a rotation matrix for the rotation parametrization as used in [2].

A.1 Restriction to inplane motion

In order to be consistent with the work presented in [2], the 2D equations are written based on the *displacements* $\mathbf{u}_0$ instead of the *positions* $\mathbf{x}_0$. Note, however, that the equations in terms of position can be recovered by making use of the relation in Eq. (3).

When restricted to motion in the (x, y) plane, there are only two nonzero components in the displacement vector $\mathbf{u}_0(s)$, namely the axial displacement u and the transverse displacement w. Based on the definition of the unit quaternion used to describe the rotation of the cross section (see Eq. (30)), only two components in $\hat{\mathbf{q}}$ are nonzero, namely q_0 and q_3 (corresponding to a rotation around the (fixed) axis in the z-direction). With the components $q_1 = q_2 = 0$ in $\hat{\mathbf{q}}$, the $\Phi_L(\hat{\mathbf{q}})$ and $\Phi_R(\hat{\mathbf{q}})$ operations used to perform the quaternion multiplication (see Eq. (28a)–(28b)) become:

$$\Phi_L\left(\hat{\mathbf{q}}\right) = \begin{bmatrix} q_0 & 0 & 0 & -q_3 \\ 0 & q_0 & -q_3 & 0 \\ 0 & q_3 & q_0 & 0 \\ q_3 & 0 & 0 & q_0 \end{bmatrix}, \quad \Phi_R\left(\hat{\mathbf{q}}\right) = \begin{bmatrix} q_0 & 0 & 0 & -q_3 \\ 0 & q_0 & q_3 & 0 \\ 0 & -q_3 & q_0 & 0 \\ q_3 & 0 & 0 & q_0 \end{bmatrix}. \tag{A.1}$$

In this case, the rotation matrix $\mathbf{R}$ as defined in Eq. (34) simplifies to:

$$\mathbf{R} = \mathbf{R}_{\hat{\mathbf{q}}} = \begin{bmatrix} 1 - 2q_3^2 & -2q_0q_3 & 0 \\ 2q_0q_3 & 1 - 2q_3^2 & 0 \\ 0 & 0 & 1 \end{bmatrix} = \begin{bmatrix} R_{11} & -R_{21} & 0 \\ R_{21} & R_{11} & 0 \\ 0 & 0 & 1 \end{bmatrix}, \tag{A.2}$$

with unity constraint: $\hat{\mathbf{q}} \cdot \hat{\mathbf{q}} = q_0^2 + q_3^2 = 1$.

A.2 2D deformation and forces

Then, according to Eq. (35a)–(35b), the strains $\hat{\mathbf{\Gamma}}$ and curvature $\hat{\mathbf{K}}$ vectors are written explicitly as:

$$\begin{aligned} \hat{\mathbf{\Gamma}} &= \begin{bmatrix} 0 \\ e \\ \gamma \\ 0 \end{bmatrix} = \begin{bmatrix} 0 \\ \left(1 - 2q_3^2\right)\left(u' + 1\right) + 2q_0q_3w' - 1 \\ -2q_0q_3\left(u' + 1\right) + \left(1 - 2q_3^2\right)w' \\ 0 \end{bmatrix}, \\ \hat{\mathbf{K}} &= \begin{bmatrix} 0 \\ 0 \\ 0 \\ \kappa \end{bmatrix} = \begin{bmatrix} 0 \\ 0 \\ 0 \\ 2q_0q_3' - 2q_3q_0' \end{bmatrix}. \end{aligned} \tag{A.3}$$

Retaining the same linear constitutive relation as in the 3D case (Eq. (41)), the stress resultants in force and moment restricted to 2D motions are written, respectively, as:

$$\begin{aligned} \hat{\mathbf{N}} &= \hat{\mathbf{C}}_N\hat{\mathbf{\Gamma}} = \begin{bmatrix} 0 \\ N \\ T \\ 0 \end{bmatrix} = \begin{bmatrix} 0 \\ EAe \\ k_yGA\gamma \\ 0 \end{bmatrix}, \\ \hat{\mathbf{M}} &= \hat{\mathbf{C}}_M\hat{\mathbf{K}} = \begin{bmatrix} 0 \\ 0 \\ 0 \\ M \end{bmatrix} = \begin{bmatrix} 0 \\ 0 \\ 0 \\ EI_z\kappa \end{bmatrix}, \end{aligned} \tag{A.4}$$

where the only nonzero elements in 2D are the axial force N, the shear force T, and the bending moment M.

A.3 Principle of virtual work

With the previous definitions, the principle of virtual work given in Eq. (50) can be simplified and written explicitly for each nonzero component. First, the variations $\delta\hat{\mathbf{\Gamma}}$ and $\delta\hat{\mathbf{K}}$ are computed from Eqs. (A.3) and reorganized into the form:

$$\begin{cases} \delta e = \left(1 - 2q_3^2\right)\delta u' + 2q_0 q_3 \delta w' - 2q_3\gamma\delta q_0 + 2q_0\gamma\delta q_3, & \text{(A.5a)} \\ \delta\gamma = -2q_0 q_3\delta u' + \left(1 - 2q_3^2\right)\delta w' + 2q_3\left(e+1\right)\delta q_0 - 2q_0\left(e+1\right), & \text{(A.5b)} \\ \delta\kappa = -2q_3'\delta q_0 + 2q_0'\delta q_3 - 2q_3\delta q_0' + 2q_0\delta q_3'. & \text{(A.5c)} \end{cases}$$

Substituting into Eq. (50) and retaining only nonzero components leads to the following explicit form of the principle of virtual work for inplane motion:

$$\int_0^L \begin{bmatrix} R_{11}N - R_{21}T \\ R_{21}N + R_{22}T \\ \rho A\ddot{u}_0 - n_e \\ \rho A\ddot{w}_0 - t_e \\ -2q_3 M \\ 2q_0 M \\ -2q_3\gamma N + 2q_3\left(e+1\right)T - 2q_3{}'M + 2\mu q_0 \\ 2q_0\gamma N - 2q_0\left(e+1\right)T + 2q_0{}'M + 2\mu q_3 \\ {q_0}^2 + {q_3}^2 - 1 \end{bmatrix}^T \begin{bmatrix} \delta u_0' \\ \delta w_0' \\ \delta u_0 \\ \delta w_0 \\ \delta q_0' \\ \delta q_3' \\ \delta q_0 \\ \delta q_3 \\ \delta\mu \end{bmatrix} \mathrm{d}s = 0, \qquad \text{(A.6)}$$

where R_{ij} are the components of the rotation matrix expressed as a function of q_0 and q_3 as defined in Eq. (A.2).

A.4 Discretization into finite elements and quadratic recast

Discretization of the 2D system into finite elements follows much of the same procedure as in the 3D case. The system is discretized into N_e elements of individual length L^e. At each node of the mesh, there are 5 degrees of freedom: the 2 displacements of the centerline (u, the axial displacement, and w, the transverse displacement), contained in $\mathbf{u}_0$, the 2 nonzero elements of $\hat{\mathbf{q}}$ (q_0 and q_3) and the Lagrange multiplier μ once governing the unity constraint. Here, quadratic functions are again used for the interpolation of the various fields, and following the same conventions established in Sect. 4, the interpolation over a single element can be written as:

$$\begin{bmatrix} u^e \\ w^e \\ q_0^e \\ q_3^e \\ \mu^e \end{bmatrix} = \mathbf{P}(s)\mathbf{z}^e, \qquad \text{(A.7)}$$

where $\mathbf{P}(s)$ is the interpolation matrix of size 5×15 with the same interpolation functions $N_1(s)$, $N_2(s)$, and $N_3(s)$ as defined in Eqs. (54a)–(54c):

$$\mathbf{P}(s) = \begin{bmatrix} N_1(s)\mathbf{I}_5 & N_2(s)\mathbf{I}_5 & N_3(s)\mathbf{I}_5 \end{bmatrix} \qquad \text{(A.8)}$$

and where $\mathbf{z}^e$ is the vector gathering all degrees of freedom for a single element defined as:

$$\mathbf{z}^e = [\underbrace{u_1 \quad w_1 \quad q_{0,1} \quad q_{3,1} \quad \mu_1}_{\text{node 1}} \quad \underbrace{u_2 \quad w_2 \quad q_{0,2} \quad q_{3,2} \quad \mu_2}_{\text{node 2}} \quad \underbrace{u_3 \quad w_3 \quad q_{0,3} \quad q_{3,3} \quad \mu_3}_{\text{node 3}}]^{\mathrm{T}}. \tag{A.9}$$

Finally, the variation of the fields (and their derivatives) over an element is rewritten under matrix form as follows:

$$\begin{bmatrix} \delta(u^e)' \\ \delta(w^e)' \\ \delta u^e \\ \delta w^e \\ \delta(q_0^e)' \\ \delta(q_3^e)' \\ \delta q_0^e \\ \delta q_3^e \\ \delta \mu^e \end{bmatrix} = \mathbf{Q}(s)\delta\mathbf{z}^e, \tag{A.10}$$

where $\delta\mathbf{z}^e$ is the variation of the element dofs and the interpolation matrix $\mathbf{Q}(s)$ (of size 9×15) is defined as:

$$\mathbf{Q}(s) = \begin{bmatrix} N_1'\mathbf{I}_2 & \mathbf{0} & \mathbf{0} & N_2'\mathbf{I}_2 & \mathbf{0} & \mathbf{0} & N_3'\mathbf{I}_2 & \mathbf{0} & \mathbf{0} \\ N_1\mathbf{I}_2 & \mathbf{0} & \mathbf{0} & N_2\mathbf{I}_2 & \mathbf{0} & \mathbf{0} & N_3\mathbf{I}_2 & \mathbf{0} & \mathbf{0} \\ \mathbf{0} & N_1'\mathbf{I}_2 & \mathbf{0} & \mathbf{0} & N_2'\mathbf{I}_2 & \mathbf{0} & \mathbf{0} & N_3'\mathbf{I}_2 & \mathbf{0} \\ \mathbf{0} & N_1\mathbf{I}_2 & \mathbf{0} & \mathbf{0} & N_2\mathbf{I}_2 & \mathbf{0} & \mathbf{0} & N_3\mathbf{I}_2 & \mathbf{0} \\ \mathbf{0} & \mathbf{0} & N_1 & \mathbf{0} & \mathbf{0} & N_2 & \mathbf{0} & \mathbf{0} & N_3 \end{bmatrix}, \tag{A.11}$$

where $\mathbf{I}_2$ represents the 2×2 identity matrix.

A.5 Discretization of the dynamic equilibrium equations

With all parameters now having been reduced to 2D from the general 3D motion, discretization of the dynamic equilibrium equations follows exactly the same procedure as presented in Sect. 4.2. For this reason, this section focuses simply on writing the principle vectors and matrices for the 2D motions, in particular the elementary mass matrix $\mathbb{M}^e$, the external force vector $\mathbf{F}^e_{\text{ext}}$, and the internal force vector, incorporating also the constraint as in Sect. 4.2, $\mathbf{F}^e_g$. Recall from Sect. 4 that to avoid shear locking, the integrals are evaluated using reduced integration: in this case, a 2-point Gauss reduced integration for 3-node elements.

To begin, the virtual inertial work is discretized (recalling that the rotational inertia is neglected), which is written:

$$\delta W_a^e = \int_0^{L^e} \rho \ddot{\mathbf{u}}_0^{e\mathrm{T}} \mathbf{A} \delta \mathbf{u}_0^e \mathrm{d}s = \delta \mathbf{z}^{e\mathrm{T}} \mathbb{M}^e \ddot{\mathbf{z}}^e, \tag{A.12}$$

where the mass matrix $\mathbb{M}^e$ (of size 15×15) can be deduced directly from that of the 3D case by discarding the rows and columns associated with the unnecessary dofs (the out-of-plane translation and the q_1, q_2 components of the quaternion).

The virtual work of the internal and the constraint forces can be gathered in the form:

$$\delta W_i^e + \delta W_\mu^e = \delta \mathbf{z}^{e\mathrm{T}} \underbrace{\int_0^{L^e} \mathbf{Q}^{\mathrm{T}} \mathbf{g}^e(\mathbf{z}^e) \mathrm{d}s}_{\mathbf{F}_{\mathrm{int}}^e}, \tag{A.13}$$

such that the elementary internal force vector $\mathbf{F}_{\mathrm{int}}^e$ can be computed using reduced integration. The expression for $\mathbf{g}^e(\mathbf{z}^e)$ is given as:

$$\mathbf{g}^e = \begin{bmatrix} \left(1 - 2q_3^{e2}\right) N^e - 2q_0^e q_3^e T^e \\ 2q_0^e q_3^e N^e + \left(1 - 2q_3^{e2}\right) T^e \\ 0 \\ 0 \\ -2q_3^e M^e \\ 2q_0^e M^e \\ -2q_3^e \gamma^e N^e + 2q_3^e \left(e^e + 1\right) T^e - 2q_3^{e\prime} M^e + 2\mu^e q_0^e \\ 2q_0^e \gamma^e N^e - 2q_0^e \left(e^e + 1\right) T^e + 2q_0^{e\prime} M^e + 2\mu^e q_3^e \\ q_0^{e2} + q_3^{e2} - 1 \end{bmatrix}. \tag{A.14}$$

Finally, the discretization of the virtual external work in 2D takes the form:

$$\delta W_e^e = \delta \mathbf{z}^{e\mathrm{T}} \underbrace{\int_0^{L^e} \mathbf{P}^{\mathrm{T}} \mathbf{f}_e^e \mathrm{d}s}_{\mathbf{F}_{\mathrm{ext}}^e}, \tag{A.15}$$

with $\mathbf{f}_e^e = \begin{bmatrix} n^e & p^e & -2q_3^e q^e & 2q_0^e q^e & 0 \end{bmatrix}^{\mathrm{T}}$ the element linear distribution of external forces and moment. Once again, the point loads at the boundaries must be taken into account in $\mathbf{F}_{\mathrm{ext}}^e$ as in 3D.

The elements are assembled for the entire structure and the full discrete finite-element model falls into the same general form Eq. (66), where the mass $\mathbb{M}$ and damping $\mathbb{D}$ matrices reduce to size $5N_n \times 5N_n$ for inplane motion.

A.6 Quadratic recast of the 2D system

When using a resolution of the dynamical system with the MANLAB package, the system should be "recast" to include only quadratic nonlinearities. To this end, 6 auxiliary variables are defined at each Gauss point of the elements as:

$$\begin{cases} R_{11}^e = 1 - 2q_3^{e2}, & \text{(A.16a)} \\ R_{21}^e = 2q_0^e q_3^e, & \text{(A.16b)} \\ e^e = R_{11}^e \left(u^{e\prime} + 1\right) + R_{21}^e w^{e\prime} - 1, & \text{(A.16c)} \\ \gamma^e = -R_{21} \left(u^{e\prime} + 1\right) + R_{11}^e w^{e\prime}, & \text{(A.16d)} \\ \kappa^e = 2q_0^e q_3^{e\prime} - 2q_3^e q_0^{e\prime}, & \text{(A.16e)} \\ v_6^e = EAe^e \gamma^e - k_z GA\gamma^e \left(e^e + 1\right). & \text{(A.16f)} \end{cases}$$

The auxiliary variables are added into the vector of degrees of freedom, which allows the vector $\mathbf{g}^e$ to be recast using only quadratic nonlinearities as:

$$\mathbf{g}^e = \begin{bmatrix} EAR_{11}^e e^e - k_y GAR_{21}\gamma^e \\ EAR_{21}^e e^e + k_y GAR_{11}\gamma^e \\ -2EI_z q_3^e \kappa^e \\ 2EI_z q_0^e \kappa^e \\ -2EI_z q_3^{e\prime}\kappa^e - 2q_3^e v_6^e + 2\mu^e q_0^e \\ 2EI_z q_0^{e\prime}\kappa^e - 2q_0^e v_6^e + 2\mu^e q_3^e \\ q_0^{e2} + q_3^{e2} - 1 \end{bmatrix}, \tag{A.17}$$

where EAe^e, $k_y GA\gamma^e$, and $EI_z\kappa^e$ have been substituted for N^e, T^e, and M^e, respectively, in Eq. (A.17).

As in the 3D case, the full first-order quadratic DAE for a single finite element can be written explicitly for the 2D inplane motions. Using 3-node elements, there are:

1. 27 primary variables:
   - 15 "displacement" degrees of freedom (5 per node) contained in $\mathbf{z}^e$ Eq. (A.9);
   - 12 "velocity" degrees of freedom (4 per node) contained in $\mathbf{V}^e$, noting that the Lagrange multiplier μ does not have a time derivative:

$$\begin{aligned} \mathbf{V}^e = \big[& V_{u_1} \;\; V_{w_1} \;\; V_{q_{0,1}} \;\; V_{q_{3,1}} \;\; V_{u_2} \;\; V_{w_2} \;\; V_{q_{0,2}} \;\; V_{q_{3,2}} \\ & V_{u_3} \;\; V_{w_3} \;\; V_{q_{0,3}} \;\; V_{q_{3,3}} \big]^{\mathrm{T}}. \end{aligned} \tag{A.18}$$

2. 12 auxiliary variables contained in $\mathbf{v}^e$ (Eqs. (A.16a)–(A.16f)) at 2 Gauss points,

such that the first-order quadratic DAE for a single finite element is written as:

$$\dot{\mathbf{z}}_-^e = \mathbf{V}^e, \tag{A.19a}$$

$$\mathbb{M}^e \dot{\mathbf{V}}_+^e = \mathbf{F}_{\text{ext}}^e - \mathbf{D}^e \mathbf{V}_+^e - \mathbf{F}_g^e, \tag{A.19b}$$

$$0 = R_{11}^e - \left(1 - 2q_3^{e2}\right), \tag{A.19c}$$

$$0 = R_{21}^e - 2q_0^e q_3^e, \tag{A.19d}$$

$$0 = e^e - R_{11}^e \left(u^{e\prime} + 1\right) - R_{21}^e w^{e\prime} + 1, \tag{A.19e}$$

$$0 = \gamma^e + R_{21}^e \left(u^{e\prime} + 1\right) - R_{11}^e w^{e\prime}, \tag{A.19f}$$

$$0 = \kappa^e - 2q_0^e q_3^{e\prime} + 2q_3^e q_0^{e\prime}, \tag{A.19g}$$

$$0 = v_6^e - EAe^e\gamma^e + k_z GA\gamma^e(e^e + 1), \tag{A.19h}$$

where, as in Sect. 4, the $\diamond_-$ notation indicates that the locations of the Lagrange multipliers μ have been removed, while $\diamond_+$ indicates that zeros have been added in $\mathbf{V}^e$ in the locations of the Lagrange multipliers to match dimensions.

For the full first-order quadratic FE DAE, the total number of degrees of freedom is $N_{\text{dof}} = 27N_n + 12N_e$. Of course, if a 2-node element with linear interpolation functions is used, fewer degrees of freedom are involved in the full quadratic DAE.

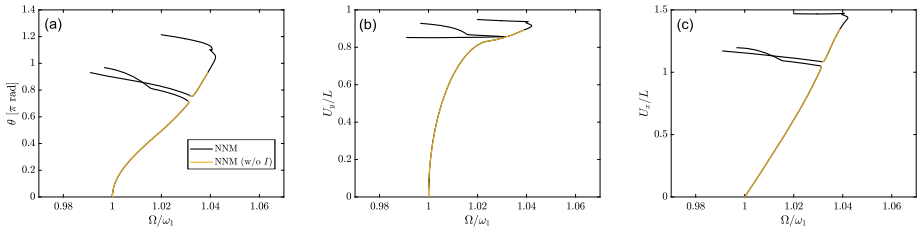

Fig. 8 Comparison of the backbone curves of the first nonlinear mode of the cantilever beam of [2] with and without rotational inertia for a beam of slenderness $\eta = 8.33 \times 10^{-8}$. (a) cross section's rotation at the end $\theta(L)$, (b) normalized axial displacement at the end $U(L)/L$, (c) normalized transverse displacement at the end $V(L)/L$

Appendix B: Effect of rotational inertia on the backbone curves of slender beams

In the work presented in this paper, rotary inertia of the beam cross section is neglected. This assumption greatly simplifies the derivation of the virtual work of the inertial forces δW_a defined in Eq. (22a) as:

$$\delta W_a = \underbrace{\int_0^L \left(\rho \mathbf{A}\ddot{\mathbf{x}}_0^{\mathrm{T}}\delta\mathbf{x}_0\right)\mathrm{d}s}_{\text{translational KE}} + \underbrace{\int_0^L \left((\mathbf{J}\dot{\boldsymbol{\Omega}} + \tilde{\boldsymbol{\Omega}}\mathbf{J}\boldsymbol{\Omega})^{\mathrm{T}}\delta\boldsymbol{\Theta}\right)\mathrm{d}s}_{\text{rotational KE}}, \tag{B.1}$$

where the translational and rotational contributions to δW_a have been identified. Neglecting the rotary inertia has the effect of removing the second term of δW_a and therefore neglects rotational inertial effects in the mass matrix (as seen by the definition of the mass matrix in Eq. (61), where zeros are added in the place of the rotation degrees of freedom).

To confirm that the rotary inertia of cross sections can indeed be neglected in the considered test cases (very slender beams), the results of a 2D simulation taking into account the rotational inertia is compared to a simulation disregarding it. To this end, the cantilever beam test case of [2], which takes into account the rotary inertia for an inplane motion, is rerun with and without the rotational inertial contributions.

Note that we choose the cantilever as a test case since it has the largest amplitude of motion of any of the systems studied in [2], meaning that any rotational inertia effects should be highest for the cantilever vibrating at large amplitude. The comparison between the simulations with and without inertia is summarized in Fig. 8.

In Fig. 8, the black backbone curves of the first cantilever mode are directly recopied from [2], while the yellow backbone curve overlaid onto Fig. 8 represents the same computation while neglecting the rotational inertia. It is clearly seen that there is no distinguishable difference between the computation with rotational inertia and without, thereby justifying the assumption of neglecting rotary inertia for the kinematics of very slender 3D beam structures.

Acknowledgements This project has received funding from the European Union's Horizon 2020 research and innovation program under the Marie Skłodowska-Curie grant agreement No. 860124. The present paper only reflects the authors' view. The European Commission and its Research Executive Agency (REA) are not responsible for any use that may be made of the information it contains.

Author contributions M. Debeurre wrote the code, carried out the numerical simulations and wrote the draft of the paper. A. Grolet helped with the code, wrote and review the draft of the paper. O. Thomas supervised the work, wrote and review the draft of the paper.

Data Availability No datasets were generated or analysed during the current study.

Declarations

Competing interests The authors declare no competing interests.

References

1. Cottanceau, E., Thomas, O., Véron, P., Alochet, M., Deligny, R.: A finite element/quaternion/asymptotic numerical method for the 3D simulation of flexible cables. Finite Elem. Anal. Des. **139**, 14–34 (2018)
2. Debeurre, M., Grolet, A., Cochelin, B., Thomas, O.: Finite element computation of nonlinear modes and frequency response of geometrically exact beam structures. J. Sound Vib. **548**, 117534 (2023)
3. Reissner, E.: On one-dimensional finite-strain beam theory: the plane problem. J. Appl. Math. Phys. **23**, 795–804 (1972)
4. Reissner, E.: On finite deformations of space-curved beams. J. Appl. Math. Phys. **32**, 734–744 (1981)
5. Simo, J.C.: A finite strain beam formulation. The three-dimensional dynamic problem. Part I. Comput. Methods Appl. Mech. Eng. **49**, 55–70 (1985)
6. Simo, J.C., Vu-Quoc, L.: A three-dimensional finite-strain rod model. Part II: computational aspects. Comput. Methods Appl. Mech. Eng. **58**, 79–116 (1986)
7. Crisfield, M.A., Jelenić, G.: Objectivity of strain measures in geometrically exact 3D beam theory and its finite-element implementation. Proc. R. Soc. Lond. **455**, 1125–1147 (1999)
8. Jelenić, G., Crisfield, M.A.: Geometrically exact 3D beam theory: implementation of a strain-invariant finite element for statics and dynamics. Comput. Methods Appl. Mech. Eng. **171**, 141–171 (1999)
9. Irschik, H., Gerstmayr, J.: A continuum mechanics based derivation of Reissner's large-displacement finite-strain beam theory: the case of plane deformations of originally straight Bernoulli–Euler beams. Acta Mech. **206**, 1–21 (2009)
10. Irschik, H., Gerstmayr, J.: A continuum-mechanics interpretation of Reissner's non-linear shear-deformable beam theory. Math. Comput. Model. Dyn. Syst. **17**(1), 19–29 (2011)
11. Meier, C., Popp, A., Wall, W.A.: Geometrically exact finite element formulations for slender beams: Kirchhoff-Love theory versus simo-Reissner theory. Arch. Comput. Methods Eng. **26**, 163–243 (2019)
12. Lázaro, C., Monleón, S., Bessini, J., Casanova, J.: A review on geometrically exact models for very flexible rods. In: Proceedings of the IASS Annual Symposium, Tokyo, Japan (2016)
13. Crisfield, M.A.: A consistent co-rotational formulation for non-linear, three-dimensional, beam-elements. Comput. Methods Appl. Mech. Eng. **81**, 131–150 (1990)
14. Crisfield, M.A., Galvanetto, U., Jelenić, G.: Dynamics of 3-D co-rotational beams. Comput. Mech. **20**, 507–519 (1997)
15. Gerstmayr, J., Shabana, A.A.: Analysis of thin beams and cables using the absolute nodal co-ordinate formulation. Nonlinear Dyn. **45**, 109–130 (2006)
16. Gerstmayr, J., Matikainen, M., Mikkola, A.: A geometrically exact beam element based on the absolute nodal coordinate formulation. Multibody Syst. Dyn. **20**, 359 (2008)
17. Gerstmayr, J., Schöberl, J.: A 3D finite element method for flexible multibody systems. Multibody Syst. Dyn. **15**, 305–320 (2006)
18. Shabana, A.A., Hussien, H.A., Escalona, J.L.: Application of the absolute nodal coordinate formulation to large rotation and large deformation problems. J. Mech. Des. **120**(2), 188–195 (1998). https://doi.org/10.1115/1.2826958
19. Shabana, A.A., Yakoub, R.Y.: Three dimensional absolute nodal coordinate formulation for beam elements. Theory, J. Mech. Des. **123**(4), 606–613 (2001)
20. Bauchau, O.A., Han, S., Mikkola, A., Matikainen, M.K.: Comparison of the absolute nodal coordinate and geometrically exact formulations for beams. Multibody Syst. Dyn. **32**, 67–85 (2014). https://doi.org/10.1007/s11044-013-9374-7
21. Romero, I.: A comparison of finite elements for nonlinear beams: the absolute nodal coordinate and geometrically exact formulations. Multibody Syst. Dyn. **20**(1), 51–68 (2008)
22. Eugster, S., Harsch, J.: A family of total Lagrangian Petrov–Galerkin Cosserat rod finite element formulations. GAMM-Mitt. **46**(2), e202300008 (2023). https://doi.org/10.1002/gamm.202300008
23. Harsch, J., Sailer, S., Eugster, S.: A total Lagrangian, objective and intrinsically locking-free Petrov–Galerkin SE(3) Cosserat rod finite element formulation. Int. J. Numer. Methods Eng. **123**(13), 2965–2994 (2023). https://doi.org/10.1002/nme.7236

24. Bagheri, A.K., Sonneville, V., Renson, L.: Nonlinear normal modes of highly flexible beam structures modelled under the se(3) Lie group framework. Nonlinear Dyn. **112**, 1641–1659 (2024)
25. Lang, H., Linn, J., Arnold, M.: Multi-body dynamics simulation of geometrically exact Cosserat rods. Multibody Syst. Dyn. **25**, 285–312 (2011)
26. Lang, H., Arnold, M.: Numerical aspects in the dynamic simulation of geometrically exact rods. Appl. Numer. Math. **62**, 1411–1427 (2012)
27. Farohki, H., Ghayesh, M.H.: Geometrically exact extreme vibrations of cantilevers. Int. J. Mech. Sci. **168**, 105051 (2020)
28. Farohki, H., Xia, Y., Erturk, A.: Experimentally validated geometrically exact model for extreme nonlinear motions of cantilevers. Nonlinear Dyn. **107**, 457–475 (2022)
29. Romero, I., Armero, F.: An objective finite element approximation of the kinematics of geometrically exact rods and its use in the formulation of an energy–momentum conserving scheme in dynamics. Int. J. Numer. Methods Eng. **54**(12), 1683–1716 (2002). https://doi.org/10.1002/nme.486
30. Leyendecker, S., Betsch, P., Steinmann, P.: Objective energy-momentum conserving integration for the constrained dynamics of geometrically exact beams. Comput. Methods Appl. Mech. Eng. **195**, 2313–2333 (2006)
31. Zupan, E., Saje, M., Zupan, D.: Quaternion-based dynamics of geometrically nonlinear spatial beams using the Runge–Kutta method. Finite Elem. Anal. Des. **54**, 48–60 (2012). https://doi.org/10.1016/j.finel.2012.01.007
32. Brüls, O., Cardona, A., Arnold, M.: Lie group generalized-α time integration of constrained flexible multibody systems. Mech. Mach. Theory **48**, 121–137 (2012)
33. Sonneville, V., Cardona, A., Brüls, O.: Geometrically exact beam finite element formulated on the special Euclidean group SE(3). Comput. Methods Appl. Mech. Eng. **268**, 451–474 (2014)
34. Rong, J., Wu, Z., Liu, C., Brüls, O.: Geometrically exact thin-walled beam including warping formulated on the special Euclidean group se(3). Comput. Methods Appl. Mech. Eng. **369**, Article ID 113062 (2020)
35. Farokhi, H., Erturk, A.: Three-dimensional nonlinear extreme vibrations of cantilevers based on a geometrically exact model. J. Sound Vib. **510**, Article ID 116295 (2021)
36. Thomas, O., Sénéchal, A., Deü, J.-F.: Hardening/softening behavior and reduced order modeling of nonlinear vibrations of rotating cantilever beams. Nonlinear Dyn. **86**, 1293–1318 (2016)
37. Bauchau, O.: Flexible Multibody Dynamics. Solid Mechanics and Its Applications. Springer, Berlin (2011)
38. Géradin, M., Cardona, A.: Flexible Multibody Dynamics: A Finite Element Approach. Wiley, Chichester (2001)
39. Géradin, M., Cardona, A.: Kinematics and dynamics of rigid and flexible mechanisms using finite elements and quaternion algebra. Comput. Mech. **4**, 115–135 (1989)
40. Romero, I.: The interpolation of rotations and its application to finite element models of geometrically exact rods. Comput. Mech. **34**, 121–133 (2004)
41. Ghosh, S., Roy, D.: Consistent quaternion interpolation for objective finite element approximation of geometrically exact beam. Comput. Methods Appl. Mech. Eng. **198**, 555–571 (2008)
42. Zupan, E., Saje, M., Zupan, D.: The quaternion-based three-dimensional beam theory. Comput. Methods Appl. Mech. Eng. **198**, 3944–3956 (2009)
43. Zupan, E., Saje, M., Zupan, D.: The Rotational Quaternion-Based Beam FEM Formulations. Proceedings of the European Congress on Computational Methods in Applied Sciences and Engineering. ECCOMAS, Vienna (2012)
44. Chandrashekhara, S.K., Zupan, D.: Path following using velocity-based approach in quasi-static analysis. Int. J. Solids Struct. **275**, Article ID 112292 (2023)
45. Celledoni, E., Marthinsen, H., Owren, B.: An introduction to Lie group integrators - basics, new developments and applications. J. Comput. Phys. **257**, 1040–1061 (2014). https://doi.org/10.1016/j.jcp.2012.12.031
46. Antman, S.S.: Nonlinear Problems of Elasticity. Springer, Berlin (1995)
47. Linn, J., Lang, H., Tuganov, A.: Geometrically exact Cosserat rods with Kelvin-Voigt type viscous damping. Mech. Sci. **4**, 79–96 (2013)
48. Kapania, R.K., Li, J.: On a geometrically exact curved/twisted beam theory under rigid cross-section assumption. Comput. Mech. **30**, 428–443 (2003)
49. Wriggers, P.: Nonlinear Finite Element Methods. Springer, Berlin (2008)
50. Géradin, M., Rixen, D.: Mechanical Vibrations, Theory and Application to Structural Dynamics. Wiley, New York (2015)
51. Mindlin, R.D.: Influence of rotatory inertia and shear on flexural motions of isotropic, elastic plates. J. Appl. Mech. **18**(1), 31–38 (1951)
52. Dill, E.: Kirchhoff's theory of rods. Arch. Hist. Exact Sci. **44**, 1–23 (1992)

53. Salamin, E.: Applications of quaternions to computation with rotations Working Paper, Stanford AI Lab (1979)
54. Bathe, K.: Finite Element Procedures. K.J. Bathe, Watertown (2014)
55. Cochelin, B., Vergez, C.: A high order purely frequency-based harmonic balance formulation for continuation of periodic solutions. J. Sound Vib. **324**, 243–262 (2009)
56. Guillot, L., Cochelin, B., Vergez, C.: A Taylor series-based continuation method for solutions of dynamical systems. Nonlinear Dyn. **98**, 2827–2845 (2019)
57. Cochelin, B.: A path following technique via an asymptotic-numerical method. Comput. Struct. **53**(4), 1181–1192 (1994)
58. Karkar, S., Cochelin, B., Vergez, C.: A high-order, purely frequency based harmonic balance formulation for continuation of periodic solutions: the case of non-polynomial nonlinearities. J. Sound Vib. **332**(4), 968–977 (2009)
59. Debeurre, M., Grolet, A., Thomas, O.: Extreme nonlinear dynamics of cantilever beams: effect of gravity and slenderness on the nonlinear modes. Nonlinear Dyn. **111**, 12787–12815 (2023). https://doi.org/10.1007/s11071-023-08637-x
60. Givois, A., Grolet, A., Thomas, O., Deü, J.-F.: On the frequency response computation of geometrically nonlinear flat structures using reduced-order finite element models. Nonlinear Dyn. **97**(2), 1747–1781 (2019)
61. Martin, A., Opreni, A., Vizzaccaro, A., Debeurre, M., Salles, L., Frangi, A., Thomas, O., Touzé, C.: Reduced order modeling of geometrically nonlinear rotating structures using the direct parametrisation of invariant manifolds. J. Theor. Comput. Appl. Mech. (2023). https://doi.org/10.46298/jtcam.10430
62. Cusumano, J.P., Moon, F.C.: Chaotic non-planar vibrations of the thin elastica, part I: experimental observation of planar instability. J. Sound Vib. **179**(2), 185–208 (1995)
63. Santillan, S., Plaut, R., Witelski, T., Virgin, L.: Large oscillations of beams and columns including self-weight. Int. J. Non-Linear Mech. **43**, 761–771 (2008)
64. Kerschen, G., Peeters, M., Golinval, J., Vakakis, A.: Nonlinear normal modes, part I: a useful framework for the structural dynamicist. Mech. Syst. Signal Process. **23**, 170–194 (2009)
65. Vincent, P., Descombin, A., Dagher, S., Seoudi, T., Lazarus, A., Thomas, O., Ayari, A., Purcell, S.T., Perisanu, S.: Nonlinear polarization coupling in freestanding nanowire/nanotube resonators. J. Appl. Phys. **125**, Article ID 044302 (2019)
66. Shen, Y., Vizzaccaro, A., Kesmia, N., Yu, T., Salles, L., Thomas, O., Touzé, C.: Comparison of reduction methods for finite element geometrically nonlinear beam structures. Vibration **4**, 175–204 (2021)
67. Givois, A., Tan, J.-J., Touzé, C., Thomas, O.: Backbone curves of coupled cubic oscillators in one-to-one internal resonance: bifurcation scenario, measurements and parameter identification. Meccanica **55**(3), 481–503 (2020). https://doi.org/10.1007/s11012-020-01132-2
68. Crespo da Silva, M.R.M., Glynn, C.C.: Nonlinear flexural-flexural-torsional dynamics of inextensible beams. I. equations of motion. J. Struct. Mech. **6**, 437–448 (1978)
69. Crespo da Silva, M.R.M., Glynn, C.C.: Nonlinear flexural-flexural-torsional dynamics of inextensible beams. II. Forced motions. J. Struct. Mech. **6**, 449–461 (1978)
70. Benacchio, S., Chatelain, P., Giraud-Audine, C., Thomas, O.: Mesure de résonances non linéaires et de courbes maîtresses pour des poutres excitées paramétriquement. In: Proceedings of the 15ème Colloque National en Calcul des Structures Hyères-les-Palmiers, France (2022)
71. Colin, M., Thomas, O., Grondel, S., Cattan, E.: Very large amplitude vibrations of flexible structures: experimental identification and validation of a quadratic drag damping model. J. Fluids Struct. **97**, Article ID 103056 (2020)